RESEARCH ARTICLE

Implementing the HYbrid MAss flux Convection Scheme (HYMACS) in ICON – First idealized tests and adaptions to the dynamical core for local mass sources

M. Langguth[1,2] | V. Kuell[1] | A. Bott[1]

[1]Institute for Geosciences, University of Bonn, Bonn, Germany

[2]Now at Juelich Supercomputing Centre (JSC), Forschungszentrum Juelich, Juelich, Germany.

Correspondence
M. Langguth, Juelich Supercomputing Centre (JSC), Forschungszentrum Juelich, Wilhelm-Johnen-Straße, D-52425 Juelich, Germany
Email: m.langguth@fz-juelich.de

Abstract

In this study, the Hybrid MAss flux Convection Scheme (HYMACS) is implemented in the ICOsahedral Non-hydrostatic (ICON) weather prediction model. In contrast to conventional convection parametrization schemes, the convective up- and downdrafts are solely treated as subgrid-scale processes in HYMACS, whereas the environmental subsidence is passed to the grid-scale dynamics of the hosting model. It is shown that the operational anisotropic divergence damping in ICON distorts the grid-scale dynamical response on the net mass transport parametrized by HYMACS. Thus, a revised numerical filter configuration is developed which focuses on both the compatibility to local mass sources (sinks) and the effective suppression of numerical modes inherent from the model's triangular grid. Evaluation of Jablonowski–Williamson dynamical core experiments reveal that the combination of an isotropic second-order divergence damping with a modified version of the fourth-order divergence damping outperforms against numerical filters based on diffusion. The obtained results are similar to the operational set-up indicating just a minor effect on the properties of the dynamical core. Moreover, a series of dry mass lifting experiments with the revised numerical filter confirms its compatability with HYMACS. The distortion of the grid-scale circulation is removed while gravity waves are still retained despite the potentially degenerative effect of the fourth-order divergence damping. Analyses of kinetic energy spectra confirm the effective suppression of checkerboard noise for a wide range of different situations. The present study may be understood as a base for future applications of HYMACS with a full cloud model in real-case studies.

KEYWORDS
atmospheric convection, grey zone parametrization, local mass sources, numerical filters

1 | INTRODUCTION

Over decades, cumulus convection could be safely treated as a subgrid-scale process. The (horizontal) grid spacing in the atmospheric models were too coarse ($\Delta x \gtrsim 50$ km) to represent explicitly the dynamics of individual cells which comprise narrow up- and downdraughts as well as compensational subsidence in the environment. Thus, it was justified to assume that a single grid column may contain a sample of convective clouds which at the same time only cover a small fraction of the horizontal grid area. With this assumption, the parametrization of the grid-scale effect of convective clouds can be determined by a spectral cloud ensemble (Arakawa and Schubert, 1974) or, more commonly, by a representative plume (e.g., Fritsch and Chappell 1980; Tiedtke 1989; Kain and Fritsch 1990; Betts and Miller 1993; Bechtold *et al.*, 2001, etc.).

However, due to the continuous increase in computational power and the successive refinement of the grid spacing in atmospheric models, fundamental assumptions made in conventional cumulus parametrization schemes (CPSs) have to be challenged. For instance, with $\Delta x \lesssim 10$km, the assumption of negligible up- and downdraught area fractions within the grid box, or the assumption that the horizontally non-local structure of convection is a subgrid-scale feature, are likely to be improper (Arakawa, 2004; Arakawa *et al.*, 2011). Thus, contemporary numerical weather prediction (NWP) and climate models suffer from an artificial scale separation within the so-called *convective grey zone* as convective processes have both a subgrid- and a grid-scale character. A fully explicit representation of convection as a grid-scale process would require a grid spacing in the order of 100 m (Bryan *et al.*, 2003).

This scale separation problem leads to contradictory opinions concerning the use of a CPS in real modelling applications. Several studies highlight the better organization and propagation of mesoscale convective systems as well as an improved representation of the diurnal cycle of precipitation in *convection-permitting* simulations (i.e., with deactivated parametrization of deep convection) with a grid spacing of $\Delta x \approx 5$ km (e.g., Kain *et al.*, 2008; Weisman *et al.*, 2008; Holloway *et al.*, 2012; Marsham *et al.*, 2013). Some studies even provide evidence for improvements against parametrized deep convection at $\Delta x \geq 10$ km (e.g., Pearson *et al.*, 2014; Stein *et al.*, 2015) which is occasionally further related to a better moisture–convection feedback on the Madden–Julian oscillation in the Tropics (e.g., Holloway *et al.*, 2013; Miyakawa *et al.*, 2014). While the benefit of convection-permitting simulations in the convective grey zone can be partly attributed to a stronger coupling of convective systems with the explicitly resolved flow, the

need of parametrized deep convection at $\Delta x \lesssim 10$ km is also documented. As pointed out by Malardel and Wedi (2016), a transition to a full explicit representation of deep convection at grey zone resolutions may result in unrealistic energy spectra. Their finding is supported by Deng and Stauffer (2006) and Lean *et al.* (2008), who note the occurrence of unphysical gridpoint storms (excessive peak rainfall rates) in simulations with a grid spacing of $\Delta x = 4$ km. By contrast, the parametrization of shallow convection (non-precipitating convective clouds with smaller vertical extent) is commonly not disputed with $\Delta x \approx 2$–10 km.

Hence, over recent years numerous approaches have been developed to face the representation problem of (deep) convection within the grey zone. While there are also ideas to couple a 2D *cloud-resolving* model into each grid column of a coarser hosting model in order to calculate the grid-scale effects (Grabowski and Smolarkiewicz, 1999; Grabowski, 2001), conventional CPSs have been modified to become more scale-adaptive. These adaptions may comprise the introduction of stochastics in order to reflect the subsampling problem with small grid boxes (e.g., Plant and Craig 2008; Bengtsson *et al.*, 2013), a prognostic treatment of parametrized convection with convective memory (e.g., Gerard and Geleyn 2005; Park 2014) or the reduction of the convective fluxes depending on an estimation of the updraught fraction (e.g., Han *et al.*, 2017; Kwon and Hong 2017) as proposed by the unified parametrization framework described in Arakawa and Wu (2013). It is noteworthy that some parametrization schemes also combine the latter adaption with the stochastic or the convective memory approach (e.g., Grell and Freitas 2014 and Gerard 2015, respectively).

Kuell *et al.* (2007) introduced the Hybrid MAss flux Convection Scheme (HYMACS) into the regional, non-hydrostatic COSMO (Consortium for Small-Scale Modeling) model (Baldauf *et al.*, 2011; Doms *et al.*, 2011; Doms and Baldauf, 2015). Following a suggestion by Kain and Fritsch (1993), the hybrid approach abandons the assumption of compensating subsidence as part of the subgrid-scale dynamics to be parametrized. Instead, only the smaller up- and downdraughts are subject to the hybrid CPS, whereas the environmental subsidence is passed to the grid-scale dynamics via local density tendencies through a net mass transfer between grid boxes within a grid column.

Subsequent studies revealed that HYMACS is able to improve the simulation of precipitation patterns in idealized tests (Kuell and Bott, 2008) and under various synoptic situations over Europe with the COSMO model using $\Delta x \simeq 7$ km (Kuell and Bott, 2009; 2011; 2019). Meanwhile, the hybrid approach has also been tested in other hosting models. Ong *et al.* (2017) modified the Kain–Fritsch convection scheme (Kain and Fritsch, 1990; 1993; Kain,

2004) to allow a net convective mass transport and conducted idealized tropical cyclone experiments with the Weather Research and Forecasting (WRF) model. They find that the hybrid approach is less sensitive to changes in the grid spacing and has potential benefits on tropical cyclone dynamics. Recently, Malardel and Bechtold (2019) also report on improved simulation results with the IFS model in the grey zone of deep convection ($\Delta x \lesssim$ 5 km in the spectral model) in comparison with the operational Bechtold–Tiedtke convection scheme (Tiedtke, 1993; Bechtold *et al.*, 2014) although some challenges arise with a hydrostatic modelling system.

The improvements compared to conventional CPSs can be attributed to a stronger coupling between the parametrized convection and the grid-scale flow. This coupling gets an explicit three-dimensional character via induced divergence/convergence patterns and the local mass sources/sinks also result in a pronounced gravity wave signal (e.g., Chagnon and Bannon 2005 give a theoretical investigation of mass sources in comparison to local heat sources). Gravity waves are known to be crucial for the environmental adjustment process as well as for the organization of convection (e.g., Bretherton and Smolarkiewicz 1989; Mapes *et al.*, 2003; Lane and Zhang 2011).

Recently, the ICOsahedral Non-hydrostatic (ICON) model was jointly developed by the German Weather Service (Deutscher Wetterdienst, DWD) and the Max Planck Institute for Meteorology (MPI-M). The development of ICON targets a unified modelling system for a wide range of applications comprising climate as well as global and regional NWP modelling (Wan *et al.*, 2013; Zaengl *et al.*, 2015; Crueger *et al.*, 2018; Giorgetta *et al.*, 2018). ICON may even be used for large-eddy simulations (LESs) provided a suitable modification of the physics package (special turbulence and microphysics scheme) is incorporated (Dipankar *et al.*, 2015; Heinze *et al.*, 2017). Presently the global model version of ICON as well as the refined regional subdomain over Europe (ICON-EU nest) are operationally used at DWD whereby ICON-EU nest serves as a driver for the high-resolution forecasts over Germany with the COSMO-DE ($\Delta x \simeq 2.8$ km) and the COSMO-D2 ($\Delta x \simeq 2.2$ km) model. In the near future a limited-area model application of ICON (ICON-D2) will replace COSMO-D2 (Rieger, 2018).

The full transition from COSMO to ICON and the focus on model applications with variable grid resolutions provide an excellent framework for a CPS such as HYMACS which faces the above-mentioned conceptual problems within the convective grey zone. Unfortunately, as pointed out in the subsequent sections, the implementation of HYMACS into ICON is not straightforward. The parametrized net mass transport requires a revised physics–dynamics coupling whose implementation also demands a careful reconfiguration of the numerical filter within the dynamical core of the hosting model. Thus, this work focuses on adapting ICON's numerical filter for ensuring a proper dynamical response to local mass sources and sinks without degrading its well-tested performance in common benchmark tests. The advancement of HYMACS in terms of its cloud model and closure will be addressed in a subsequent paper.

The present paper is organized as follows. Section 2 reviews the theoretical concept of HYMACS and highlights the differences with respect to conventional CPSs. Section 3 comprises a short model description of ICON, elucidates details of the physics–dynamics coupling and sketches the problems of handling local mass sources/sinks in conjunction with the operational numerical filter used in the new hosting model. Based on a short discussion on the inherent checkerboard problem of a triangular grid, revised numerical filter configurations are tested and compared in Jablonowski–Williamson test cases in Section 4. The obtained numerical filter set-up is then evaluated in Section 5 in dry mass transfer experiments with ICON, which confirm a proper dynamical flow response and effective checkerboard noise reduction. Their significance for more realistic applications is also debated in this section. A conclusion complemented by a discussion on potential further developments of HYMACS is given in Section 6.

2 | THE CONCEPT OF HYMACS

Classical CPSs rely on the assumption that no net mass transport due to convection takes place within a given grid column of the hosting model. Thus, in each grid column the mass fluxes realized by small up- and downdraughts of the convective cells are completely compensated by local subsidence (also sometimes termed as *pseudo-subsidence*). With smaller grid spacings used in contemporary NWP and climate models, this assumption has become more and more questionable, as already mentioned by Kain and Fritsch (1993). Hence, in contrast to the classical CPS schemes, the hybrid approach abandons this assumption and treats the environmental subsidence as a grid-scale process. Since a net mass transfer is not possible with the conventional Reynolds averaging formalism by definition (e.g., Arakawa *et al.*, 2011), this approach has to be abandoned necessarily.

In the following, we review in detail the concept of the hybrid mass convection scheme HYMACS. Its special properties compared to classical CPSs are highlighted and the derivation of the convective tendencies is briefly described. While referring to the ideas introduced in Kuell *et al.* (2007), the following explanations draw on

the concept of fluid volumes and its integral properties. Zdunkowski and Bott (2003) give more information on this concept.

As a starting point for the derivation of the convective fluxes, we consider an arbitrary fluid volume moving in space and time with its barycentric velocity $\mathbf{v}_b$. The volume consists of an environmental part which moves with the environmental velocity $\mathbf{v}_e$ and of a convective part (i.e., some up- or downdraught area) moving with the convective velocity $\tilde{\mathbf{v}}_c$. Writing the convective velocity as $\tilde{\mathbf{v}}_c = \mathbf{v}_e + \mathbf{v}_c$, the barycentric velocity is defined by

$$\rho\mathbf{v}_b = \rho_e\mathbf{v}_e + \rho_c(\mathbf{v}_e + \mathbf{v}_c)$$
$$= \rho\mathbf{v}_e + \mathbf{J}_c, \qquad (1)$$

with $\rho = \rho_e + \rho_c$. Here, ρ_e and ρ_c denote the partial densities of the environmental and convective volume parts, respectively, and ρ is the total density (also including water in different phase states). Within a hosting NWP model, the terms $\mathbf{v}_e$ and ρ are considered to be grid-scale quantities for which prognostic equations are solved (i.e., $\mathbf{v}_e$ is denoted as the grid-scale $\mathbf{v}$ for modelling). In contrast to this, the convective mass flux per unit area $\mathbf{J}_c = \rho_c\mathbf{v}_c$ is the subgrid-scale quantity to be parametrized with HYMACS.

The significance of $\mathbf{J}_c$ becomes obvious when evaluating the continuity equation of the regarded fluid volume

$$0 = \frac{\partial\rho}{\partial t} + \nabla\cdot(\rho\mathbf{v}) = \frac{\partial\rho}{\partial t} + \nabla\cdot(\rho\mathbf{v}_e) + \nabla\cdot\mathbf{J}_c. \qquad (2)$$

Hence, a local temporal change in density can be realized by

1. Mass flux divergence of the environmental flow, and by
2. Mass flux divergence of the convective flux.

The former can be interpreted as a consequence of spatial variations in the *grid-scale* mass flux and is calculated in the dynamical core of the hosting model. The latter accounts for the *subgrid-scale* convective mass fluxes which are not explicitly resolvable by the model and therefore need to be parametrized.

Finally, the convective density tendency can be related to the mass fluxes in the up- and downdraught region $M_{u,d}$ (in kg·s^{-1}) by assuming that convection is dominated by vertical motions, that is, $w_c \gg u_c$. This assumption is well justified by the nature of convection as the draught area is usually only a few hundred metres wide, while the draughts can penetrate the troposphere over several kilometres:

$$\left.\frac{\partial\rho}{\partial t}\right|_{conv} = -\nabla\cdot\mathbf{J}_c = -\frac{1}{A}\left(\frac{\partial M_u}{\partial z} + \frac{\partial M_d}{\partial z}\right), \qquad (3)$$

where A denotes the horizontal area of a particular grid box. Since the convective density tendency is solely determined by the vertical change of the updraught and downdraught mass flux, the mass within a convective column is conserved.

As usual, the layer-integrated entrainment rates $\epsilon_{u,d}$ and detrainment rates $\delta_{u,d}$ (in kg·s^{-1}) guide the mass flux of the up- and downdraughts so that Equation (3) can be discretized as

$$\left.\frac{\partial\rho}{\partial t}\right|_{conv} = -\frac{1}{A\Delta z}(\epsilon_{u,d} - \delta_{u,d}), \qquad (4)$$

with Δz denoting the depth of the corresponding model layer.

It is important to note that, contrary to conventional cumulus parametrization schemes, only the small-scale up- and downdraughts are parametrized in HYMACS through properly defined exchange rates with the environmental fluid. Formally, this means that the (grid-scale) average of the (subgrid) fluctuations of the vertical wind does not vanish anymore, that is, $\overline{w'} \neq 0$. Thus, the subgrid transports cannot be derived from a Reynolds averaging formulation. Instead, the hybrid approach may be viewed as an extension of classical CPSs resembling the multifluid framework introduced by Thuburn *et al.* (2018). By allowing a net mass transfer between the convective and the environmental fluid volume parts (their equation (44)), the resolved dynamics can control how the environmental subsidence is distributed instead of being confined to the local grid column.

In addition to the local change in density due to convection, HYMACS also parametrizes a convective transport of heat, moisture and momentum (Kuell *et al.*, 2007; Kuell and Bott, 2011). While these transports are a common property of CPSs, there are some distinct differences due to the net mass transfer.

To further highlight this issue, we examine the change in time of a conserved property Ψ in the fluid volume. In analogy to the considerations above, the corresponding balance equation reads

$$\frac{\partial}{\partial t}(\rho\psi) + \nabla\cdot(\mathbf{v}_e\rho\psi) + \nabla\cdot\mathbf{J}_c^\psi = -\nabla\cdot\mathbf{F}_\psi + Q_\psi, \qquad (5)$$

with $\rho\psi$ the density of the property Ψ. The specific value ψ can be, for example, the enthalpy h or any specific moisture species q_k and may also be affected by the divergence of non-convective fluxes $-\nabla\cdot\mathbf{F}_\psi$ (e.g., radiation or diffusion fluxes) and internal sources Q_ψ (e.g., latent heat release or condensation).

While the latter two terms have to be parametrized by other physical parametrizations, the term of interest for HYMACS is the divergence of the convective flux $\mathbf{J}_c^\psi$. Since

$\nabla \cdot \mathbf{J}_c^\psi$ is again guided by the layer-integrated entrainment and detrainment rates $\epsilon_{u,d}$ and $\delta_{u,d}$ respectively, we write in analogy to Equations (3) and (4)

$$\frac{\partial}{\partial t}(\rho\psi)\bigg|_{conv} = -\nabla \cdot \mathbf{J}_c^\psi$$
$$= -\frac{1}{A\Delta z}(\epsilon_{u,d}\psi - \delta_{u,d}\psi_{u,d}), \qquad (6)$$

where $\psi_{u,d}$ denote the specific values of ψ of the parametrized up- and downdraughts. Note that the grid-scale specific value ψ is used for handling the entrainment which corresponds to the approximation $\psi_e \approx \psi$. Although this is is a common hypothesis in CPSs, its validity becomes questionable with smaller grid boxes in the convective grey zones and is therefore subject to the challenge of multiscale modelling of moist convection (Arakawa and Wu, 2013). However, we need to determine how the specific value of ψ changes locally due to convection. Following Kuell *et al.* (2007), the convective tendency of ψ can finally be discretized as

$$\frac{\partial\psi}{\partial t}\bigg|_{conv} = \left(\frac{\rho(t^n)}{\rho^\star} - 1\right)\frac{\psi(t^n)}{\Delta t}$$
$$- \frac{1}{A\Delta z\rho^\star}(\epsilon_{u,d}\psi - \delta_{u,d}\psi_{u,d}), \qquad (7)$$

where $\rho^\star$ is the updated density due to a parametrized net mass transfer. The conservation property of the discretized convective ψ-tendency is briefly demonstrated in Appendix A1..

From Equation (7) it is seen that the convective ψ-tendency consists of two terms. Thus, in addition to the changes due to internal sources and non-convective fluxes, a local temporal change in ψ can be realized by

1. Advection of ψ with the environmental flow, that is, *grid-scale* advection (Equation (5)),
2. Convective mass flux divergence (first term in Equation (7)), and
3. Divergence of the convective flux of ψ (second term in Equation (7)).

Owing to the direct manifestation of the net mass transfer in the convective tendency of any quantity ψ, it is also obvious that the coupling of HYMACS in a hosting model differs from coupling a conventional CPS. In contrast to the conventional approach, this coupling can neither be isobaric, as in the COSMO model (Kuell *et al.*, 2007; Doms *et al.*, 2011), nor isochoric as in ICON (Zaengl *et al.*, 2015, hereafter abbreviated Z15). In fact, the convective density tendency has to be accounted for whenever a transformation of convective tendencies to the prognostic equations of the hosting model is required (also Section 3.2).

3 | IMPLEMENTATION OF HYMACS IN ICON

The hybrid mass flux convection scheme at hand was designed for use in nonlinear, non-hydrostatic and fully compressible NWP models such as the regional COSMO model. Thus, the following section deals with the implementation of HYMACS in the ICON model emphasizing special aspects and difficulties to be considered for this approach.

3.1 | The ICON model

As already suggested by the acronym of the modeling framework ICON, the model grid is based on the projection of an icosahedron on the sphere. By successive steps of subdivision of the twenty equilateral native triangles, triangular grid cells of different size can be obtained (*Delaunay triangulation*). In the first step of mesh refinement (root division), every triangular edge is divided into n equal sections. The division points are then connected by great circle arcs in order to form n^2 triangles. At this stage, it is worth mentioning that the resulting triangular cells are more or less distorted, especially near the vertices of the native icosahedron and hence are no longer equilateral. As a second step of mesh refinement, k bisection steps can be performed. The bisection step comprises the connection of the triangle edge midpoints, each yielding four new triangles in the parent grid cell. The final result is a triangular spherical RnBk grid (i.e., n root sections, k bisections) which consists of

$$n_C = 20n^2 4^k; \qquad n_E = 30n^2 4^k; \qquad n_V = 10n^2 4^k + 2 \quad (8)$$

cells, edges and vertices.

The operational model configuration at DWD makes use of a global R03B07 grid with a regional nest over Europe (R03B08 grid). Denoting the square root of the averaged cell area $\overline{A}_C$ on the sphere with radius $r_E = 6,371$ km, the grid spacing Δx_{ICON} can be defined by

$$\Delta x_{ICON} = \sqrt{\overline{A}_C} = \sqrt{(4\pi r_E^2)/n_C} = \sqrt{\frac{\pi}{5}}\frac{r_E}{n2^k}. \qquad (9)$$

Thus, the grid spacing of the above-mentioned grid configuration is approximately 13 and 6.5 km. On the one hand, the icosahedral triangular grid has some clear advantages. The pole problem commonly met on spherical grids is solved by a quasi-uniform coverage of the sphere by triangular cells, while the above-mentioned bisection steps allow for straightforward nesting options (e.g., Wan *et al.*, 2013 and Z15). On the other hand, the triangular cells

suffer from being distorted near the edges of the native icosahedron. While the problem of irregularity, which is crucial when discretizing spatial differential operators, can be minimized by a spring dynamics optimization (Tomita *et al.*, 2001), it remains a potential source of numerical errors near the edges of the native icosahedron (Wan *et al.*, 2013). Another problem related to triangular grids is a checkerboard pattern in the divergence field (Gassmann, 2011). The latter undesired property in particular will be discussed in more detail in the subsequent sections.

In the following, a brief overview over the prognostic equation system of ICON is given. Since a detailed explanation of the equation system is beyond the scope of the present study, we present only information relevant to the implementation of HYMACS here. For a full model description, we refer to the corresponding articles and manuscripts in the literature (e.g., in Wan *et al.*, 2013, Z15 or Prill *et al.*, 2019).

The equation system of ICON is based on the set of prognostic variables suggested by Gassmann and Herzog (2008) for atmospheric modelling. It is assumed that the atmosphere is a two-component system of dry air and water, where the latter may exist in three different phases (vapour, liquid and solid) and may form precipitable hydrometeors. Then, using a C-grid staggering (Figure 1), the prognostic variables are the horizontal velocity component normal to the triangle edges v_n, the vertical wind w, the total density ρ including all moisture species, the Exner pressure π and the specific masses of the moisture tracers q_k.

After applying a density-weighted (Hesselberg) averaging in order to handle the turbulent flow of the atmosphere, the basic equation system reads

$$\frac{\partial v_n}{\partial t} + \frac{\partial K_{\mathrm{h}}}{\partial n} + (\zeta + f)v_{\mathrm{t}} + w\frac{\partial v_n}{\partial z}$$
$$= -c_{pd}\theta_{\mathrm{v}}\frac{\partial \pi}{\partial n} - F_s(v_n) + F_d(\mathbf{v}), \tag{10}$$

$$\frac{\partial w}{\partial t} + \mathbf{v}_{\mathrm{h}} \cdot \nabla w + w\frac{\partial w}{\partial z} = c_{pd}\theta_{\mathrm{v}}\frac{\partial \pi}{\partial z} - g + F_d(w), \tag{11}$$

$$\frac{\partial \rho}{\partial t} + \nabla \cdot (\rho\mathbf{v}) = 0, \tag{12}$$

$$\frac{\partial \pi}{\partial t} + \frac{R_{\mathrm{d}}}{c_{vd}}\frac{\pi}{\rho\theta_{\mathrm{v}}}\nabla \cdot (\mathbf{v}\rho\theta_{\mathrm{v}}) = Q_{\pi,\mathrm{dia}} + F_d(\theta_{\mathrm{v}}), \tag{13}$$

$$\frac{\partial(\rho q_k)}{\partial t} + \nabla \cdot (\rho q_k\mathbf{v}) = -\nabla \cdot (J_k\mathbf{k} + \mathbf{J}_k^{\mathrm{t}}) + I_k. \tag{14}$$

Note that the Hesselberg averaging symbols are omitted for convenience.

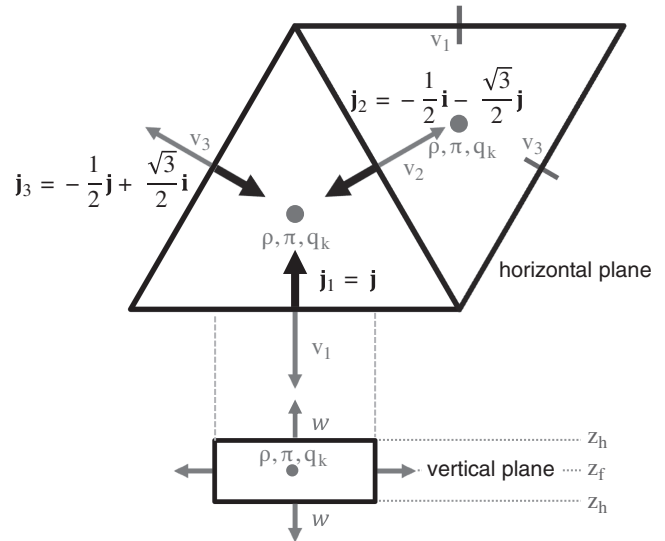In order to restrict the explanations given in this section to the essential issues of our study, we describe only

FIGURE 1 Position of ICON's prognostic variables using C-grid staggering. The basic vectors of the trivariate coordinate system and their representation with Cartesian unit vectors are also given. It is noticed that the orientation factor for upper-tip triangles f_o^{u} is -1, while for lower-tip triangles $f_o^{\mathrm{l}} = 1$ is valid

TABLE 1 Description for the remaining symbols which occur in the prognostic system (Equations (10)–(14))

Symbol	Description
v_{t}	Tangential wind component; (v_n, v_{t}, w) form a right-handed system
$K_{\mathrm{h}} = \frac{1}{2}\left(v_n^2 + v_{\mathrm{t}}^2\right)$	Horizontal kinetic energy
$\zeta = \mathbf{k} \cdot (\nabla \times \mathbf{v})$	Relative vorticity
f	Coriolis parameter
c_{pd}, c_{vd}	Specific heat of dry air at constant pressure/volume
g	Gravitational acceleration
$J_k\mathbf{k}$	Vertical diffusion flux of q_k
J_k^{t}	Turbulent flux of q_k
I_k	Source/sinks due to phase changes

the most relevant terms in the following. For the remaining symbols, we refer to the overview given in Table 1.

The thermodynamic equation expressed in terms of the Exner pressure (Equation (13)) is a reformulation of the first law of thermodynamics which can be expressed as a prognostic equation for the virtual potential temperature θ_{v} (Gassmann, 2013). This is done using the definition

$$\pi = \left(\frac{R_{\mathrm{d}}}{p_{00}}\rho\,\theta_{\mathrm{v}}\right)^{R_{\mathrm{d}}/c_{vd}} = \frac{T_{\mathrm{v}}}{\theta_{\mathrm{v}}}, \quad \text{with } \theta_{\mathrm{v}} = T_{\mathrm{v}}\left(\frac{p_{00}}{p}\right)^{R_{\mathrm{d}}/c_{pd}},$$
$$\tag{15}$$

where p is the pressure and p_{00} denotes a reference pressure. The virtual temperature T_v, also known as the density temperature, is given by

$$T_v = T(1 + \alpha) = T \{ 1 + (R_v/R_d - 1)q_v - q_{cond} \} . \quad (16)$$

Here, R_d and R_v are the gas constants for dry air and water vapour, respectively. q_v is the specific water vapour content while q_{cond} is shortcut for the sum of the specific masses of the hydrometeors (i.e., the different liquid and solid moisture species). Hence, all diabatic terms $Q_{\pi,dia}$ in Equation (13) coming from different parametrized physical processes like condensation, turbulence or convection have to be transformed to a corresponding Exner pressure tendency.

Special attention within our study is also given to the several numerical filter terms $F_d(\psi)$ with $\psi \in (\mathbf{v}, w, \theta_v)$ present in the equation system. For the prognostic equation of the Exner pressure π and the vertical wind w, the filtering comprises a Smagorinsky diffusion and a fourth-order diffusion, respectively. For details regarding these filters, we refer again to Z15.

The numerical filter for the edge-normal wind component v_n is twofold, that is,

$$F_d(\mathbf{v}) = F_{d1}(v_n) + F_{d2}(\mathbf{v}). \quad (17)$$

A Smagorinsky and a fourth-order background diffusion are combined in the first term.

$$F_{d1}(v_n) = F_{smag} + F_{diff} = 4K_s(v_n)\tilde{\nabla}^2(v_n) - k_4\tilde{\nabla}^2 \left\{ \tilde{\nabla}^2(v_n) \right\} . \quad (18)$$

While the implementation of the Smagorinsky diffusion is more physically based, the fourth-order diffusion is applied for improving simulation results with orography rather than stabilizing the dynamical core as stated by Z15. Thus, the associated damping coefficient k_4, commonly defined in terms of an "e-folding time to timestep" ratio τ_{rat}, is rather small.

The discretization of the involved Laplacian operating on v_n is a conventional centred difference approach

$$\tilde{\nabla}^2(v_n) = \frac{v_{n,2} + v_{n,1} - 2v_n}{d_{tv}^2} + \frac{v_{n,4} + v_{n,3} - 2v_n}{d_{nv}^2} \quad (19)$$

which is second-order accurate on equilateral triangles, but tends to produce discretization errors on distorted triangles near the above-mentioned pentagon points. The symbols in Equation (19) are explained in Figure 2. It is worth noting that the $v_{n,i}$ components on the neighbouring triangle vertices are retrieved by a radial basis function (RBF) reconstruction (Narcowich and Ward, 1994). For
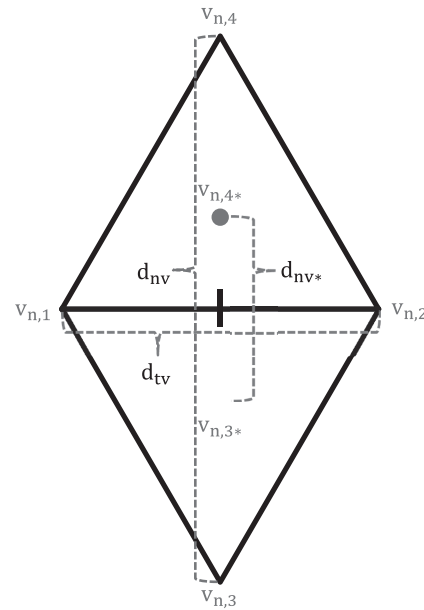

FIGURE 2 Stencil used for discretization of the Laplacian in Equation (19). The numbered normal wind components (with respect to the target v_n) are interpolated with the help of a RBF vector reconstruction. Adopted from Z15

further details on the Smagorinsky diffusion and, in particular, the computation of the associated pre-factor K_s, we refer again to the explanations given in Z15.

A fourth-order, *anisotropic* divergence damping acting on the three-dimensional divergence field (hereinafter OP4DD) serves as the second numerical filter for the horizontal momentum in Equation (17). The associated divergence damping term reads

$$F_{d2}(\mathbf{v}) = F_{div,4o} = -f_{d,4o}\overline{A}_C^2 \nabla_n \left[\mathrm{div} \left\{ \nabla_n \left(D_h + \frac{\partial w}{\partial z} \right) \right\} \right], \quad (20)$$

where $D_h = \mathrm{div}(\mathbf{v}_h)$ denotes the horizontal divergence of the velocity field. In ICON, the horizontal divergence operator 'div' is discretized using the Gauss theorem

$$\mathrm{div}(\mathbf{F}) = \frac{1}{A_C} \sum_{i=1}^{3} (F_n l_E f_o^{l,u})_i \quad (21)$$

Here, F_n is the normal component of the generic flux vector $\mathbf{F}$ given at the triangle edges of length l_E and $f_o^{l,u}$ is a corresponding orientation factor (Figure 1 gives further details on $f_o^{u,l}$). The gradient in normal direction ∇_n is discretized by a finite difference between two cell centre values adjacent to the edge of operation.

Following Z15, the divergence damping coefficient $f_{d,4o}$ normally attains values between 0.001 and 0.004 which was found to warrant numerical stability by minimizing

checkerboard noise. In the operational set-up of ICON at DWD, a relatively high value of $f_{d,4o} = 0.004$ is chosen as it proves to optimize simulation results. As already mentioned above, the problem of small-scale noise is revisited below since the operational divergence damping proves to be incompatible with the local mass sources and sinks introduced by HYMACS.

With reference to the divergence operator introduced in Equation (21) and related to the numerical filters discussed above, it is worth mentioning here that the unaveraged v_n components are used for computing D_h in the divergence damping (Equation (20)). In contrast to this, the horizontal wind vector components are averaged over a four-cell stencil in order to calculate the flux divergences appearing in the prognostic equation system (Equations (12)–(14)). The necessity for such an approach originates from the grid geometry with its appendant properties of the discretized divergence operator as detailed in Subsection 3.4.

The time integration of the equation system except for the moisture budget equation (Equations (10)–(13)) is performed by a two-time-level predictor–corrector scheme. The timestep of the scheme is limited by the propagation speed of acoustic waves and was chosen in order to ensure numerical stability up to the high stratosphere/mesosphere where wind speeds of $250 \, \mathrm{ms}^{-1}$ may be encountered at spatial resolutions resolving breaking gravity waves. Nevertheless, in order to damp non-relevant horizontal acoustic modes, the horizontal pressure gradient in Equation (10) uses an extrapolated value for the Exner pressure π taking into account the previous timestep. For terms related to vertical propagation of sound waves, an implicit scheme is used (Prill *et al.* (2019) give further details). By performing off-centring in these terms, the non-relevant vertical acoustic modes are damped as well in ICON.

To reduce the computational costs of the time integration, a time-splitting approach between the dynamical core and the physical parametrizations is applied where the physical timestep is a multiple of the dynamical timestep, that is, $\Delta t_{\mathrm{phy}} = n\Delta t_{\mathrm{dyn}}$ with $n = 5$ as a common choice. The same is also true for the prognostic equations of the moisture species (Equation (14)) except for water vapour at high levels in the stratosphere. This approach is reasonable since any fast (e.g., acoustic) modes are neither directly relevant for the parametrized processes nor for the tracer transport.

Additionally, it is worth mentioning that only the divergence damping is applied at every dynamical timestep Δt_{dyn}. More specifically, it acts on v_n as a filter term at the end of a corrector timestep. By contrast, the diffusional terms which also occur in the vertical wind and thermodynamic equation are only applied at the physics timestep

$\Delta t_{\mathrm{phy}} = n\Delta t_{\mathrm{dyn}}$ since they are not needed to ensure numerical stability following Z15.

3.2 | Physics–dynamics coupling of HYMACS in ICON

In order to reduce the computational costs of expensive physical parametrizations with relative long characteristic time-scales (e.g., radiation, but also convection), a distinction between *fast physics* and *slow physics* is made in ICON. While the tendencies of the physical processes belonging to the former group are computed at every physical timestep $\Delta t_{i,\mathrm{fast}} \equiv \Delta t_{\mathrm{phy}}$ and sequentially update the atmospheric state (known as *sequential-update split*), the latter parametrization schemes are called with a reduced frequency $\Delta t_{i,\mathrm{slow}} = n_i \Delta t_{\mathrm{phy}}$. Different integer pre-factors n_i can be specified for different physical processes where the actual specific value depends on both the time-scale of the parametrized process and the required computational costs. For convection, n_{conv} is usually chosen to yield $\Delta t_{\mathrm{conv,slow}} \approx 1$–$10$ min.

In contrast to the fast physics, the slow physics processes do not sequentially update the atmospheric state. Instead, they are fed with the state obtained from the dynamical core and updated by the fast physics processes and perform the calculations interdependently from each other (known as *parallel split*).

The resulting tendencies are then held constant over the whole period of length $\Delta t_{i,\mathrm{slow}}$ and passed to the dynamical core. The time-stepping approach is sketched in Figure 3. An overview of all physical processes and their categorization into the two different groups, i.e. slow and fast physics, can be found in Prill *et al.* (2019).

Regarding the time-split approach, HYMACS is coupled to ICON in the same way as the operational Tiedtke–Bechtold convection scheme. However, opposing to the isochoric coupling approach (assume $\rho =$ const. in the physics–dynamics interface), the net mass transfer has to be accounted for by the tendencies calculated by HYMACS.

The transfer of the convective density tendency given by Equation (4) to the dynamical core is straightforward since the continuity equation is solved explicitly.

$$\frac{\partial \rho}{\partial t} + \nabla \cdot (\rho \mathbf{v}) = \left. \frac{\partial \rho}{\partial t} \right|_{\mathrm{conv}}. \qquad (22)$$

When transforming the enthalpy tendency (given by Equation (7) in terms of the generic quantity ψ) to a corresponding change of the prognostic Exner pressure, $\partial \rho / \partial t|_{\mathrm{conv}}$ enters the transformation relation explicitly. As shown in more detail in Appendix B2., the convective
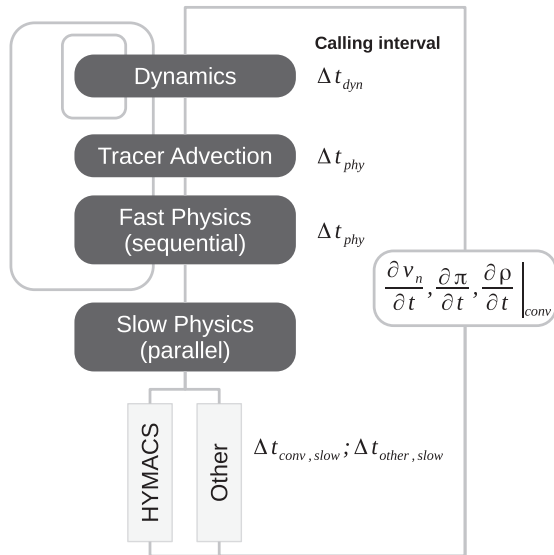
The motivation for repeating the dry mass lifting experiments with COSMO can be explained by the substantial developments of the dynamical core over the last decade. Specifically, a new fast wave solver has been implemented which also offers the use of an *isotropic* divergence damping as a numerical filter (Baldauf, 2013). This numerical filter adds appropriate damping terms in the vertical wind equation and was found to be superior for the representation of gravity waves (Gassmann and Herzog, 2007) compared to an anisotropic divergence damping (as applied in ICON). Since gravity waves are crucial for the environmental stabilization and are directly excited by local mass sources, an isotropic divergence damping is believed to be a suitable mean to ensure numerical stability and to be compatible with HYMACS.

3.3.1 | Experimental design

The mass lifting experiment proposed by Kuell *et al.* (2007) comprises the initialization of a dry, polytropic atmosphere at rest. Using a lapse rate of $6\,\mathrm{K\cdot km^{-1}}$, the background atmosphere is stably stratified. In the central grid column of the model domain, a convective cell is forced with a local mass sink at the bottom layer and an equivalent counterpart (i.e., a mass source) at a height of approximately $9\,\mathrm{km}$. In order to facilitate the analysis of emitted gravity waves, an equidistant vertical grid (e.g., $\Delta z = 300\,\mathrm{m}$) is used and the Coriolis force is neglected as well as any effects due to the curvature of the Earth (planar grid). Hence, in contrast to the idealized studies by Chagnon and Bannon (2005), no geostrophic adjustment process takes place.

In COSMO, a quadrilateral grid with a grid spacing of $\Delta x_{\mathrm{cos}} = 0.0625° \approx 6.95\,\mathrm{km}$ is used. Since ICON makes use of a triangular grid, a complete equivalent set-up is not possible. Nevertheless, for the purpose of comparison, the grid cell areas are equalized which results in an edge length of $l_{\mathrm{E}} = 10.5\,\mathrm{km}$ for the planar triangles in ICON. An (approximately) quadratic domain is chosen for both models with a domain width of about $375\,\mathrm{km}$ in order to avoid interference of emitted waves due to the double periodic boundary conditions.

In addition to the above-mentioned numerical filters (diffusion and divergence damping), a Rayleigh damping layer between the model top at $20.7\,\mathrm{km}$ and a height of $14\,\mathrm{km}$ is employed. This prevents unphysical wave reflection at the upper boundary.

The forced mass exchange in the grid column is switched on for $1\,\mathrm{hr}$ (this corresponds to an approximate life cycle of a deep convection cell) where a $60\,\mathrm{hPa}$ thick layer is overturned. Since we focus on the effect of the

FIGURE 3   Illustration of the time-stepping approach in ICON. Each grey line symbolizes a specific cycling path with a corresponding calling frequency. The two left cycling paths represent the time-stepping in the dynamical core using Δt_{dyn} as a timestep and the calculation of the tracer transport as well as the fast physics processes with Δt_{phy}. The right grey line is representative for the slow physics processes and hence related to HYMACS. Adopted from Prill *et al.*, (2019)

π-tendency is given by

$$Q_{\pi,\mathrm{dia}}\Big|_{\mathrm{conv}} \equiv \frac{\partial \pi}{\partial t}\Big|_{\mathrm{conv}} = \frac{R_{\mathrm{d}}}{c_{vd}}\frac{\pi}{\rho}\frac{\partial \rho}{\partial t}\Big|_{\mathrm{conv}} + \frac{1}{\theta_{v}}\frac{R_{\mathrm{d}}(1+\alpha)}{c_{vd}c_{pd}}\frac{\partial h}{\partial t}\Big|_{\mathrm{conv}} + \frac{R_{\mathrm{d}}\pi}{c_{vd}(1+\alpha)}\frac{\partial \alpha}{\partial t}\Big|_{\mathrm{conv}}, \qquad (23)$$

where α is the density correction term for the virtual temperature (Equation (16)).

3.3 | Dry mass lifting experiments with COSMO and ICON

When HYMACS is implemented into a hosting model, it is crucial to check that the grid-scale dynamics react properly to the local mass source and sinks introduced by our convection scheme. In order to get insight into the dynamical response to the net mass transfer, Kuell *et al.* (2007) performed dry mass lifting experiments with the COSMO model and also referred to analytical studies focusing on the effect of local mass sources like Chagnon and Bannon (2005), Gray *et al.* (1998) or Gray (1999). Since HYMACS proved to work well therein, we adopt this approach within our study and compare the subsequent modelling results obtained with ICON (version 2.3.0) with a COSMO reference simulation (version 5.1).
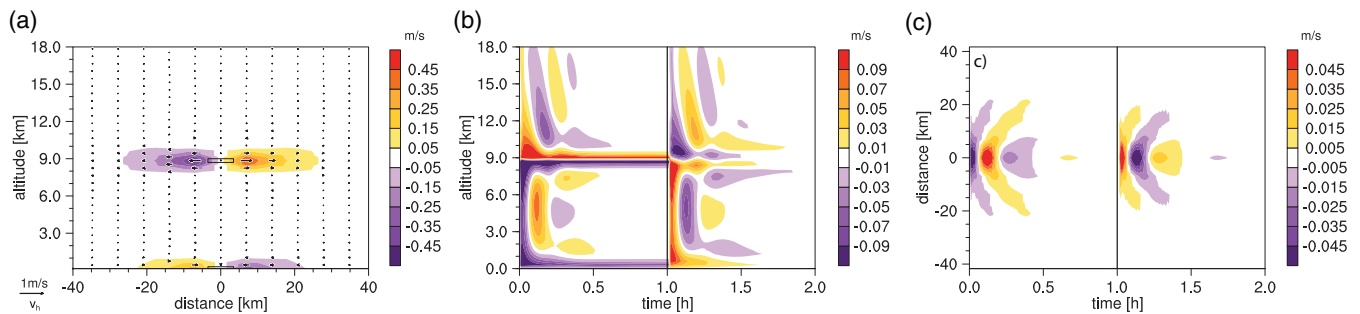
FIGURE 4 Results of the COSMO reference simulation. (a) Vertical cross-section of the u-wind through the idealized convective grid column in the zonal direction after 30 min of mass transport. The vectors show the horizontal and vertical flow while the shading shows the amplitude of the zonal wind only. The black boxes highlight the entrainment and detrainment layer. (b) shows time series of the *grid-scale* vertical wind in the convective column and (c) time series on a horizontal section at $z = 4,500$ m centred around the idealized cell. The subgrid mass transport is active for 1 hr. The end of the mass transport is highlighted by a vertical line. The results may be compared with figure 2a in Kuell *et al.* (2007)

net mass transfer, the enthalpy tendency is set to zero, although this adds some extra energy to the system.

3.3.2 | Results of the COSMO reference simulation

The results of the dry mass lifting experiment obtained with the COSMO model are summarized in Figure 4. The dynamical response due to net mass transfer comprises the following two major properties and is in good agreement with the results presented in Kuell *et al.* (2007).

When the mass transfer is switched on (off), the imposed perturbation in the resting atmosphere triggers the emission of gravity waves. These gravity waves can be readily seen as a signal in the vertical wind which propagates away from the mass source and sink in vertical and horizontal direction. The oscillating vertical wind signal in the upper levels can be attributed to the detrainment layer while, between the mass source and sink, the vertical signal is an interference of waves originating from both the entrainment (bottom) and detrainment (elevated) layers. Thus, the maximal lifting occurs at a height of 5 km at 8 min after switching on the mass transfer. The gravity wave signal propagates well over the adjacent grid columns and has an amplitude of about 0.0025 m·s^{-1} up to a distance of 20 km from the convective grid column. After a while, the vertical wind oscillations fade away and the flow pattern becomes rather stationary. Around the detrainment layer, horizontal as well as vertical divergence (i.e., a dipole in the vertical wind field) has evolved, whereas three-dimensional convergence is visible around the entrainment layer. The horizontal outflow/inflow extends well over several grid boxes and is pronounced to about $1,000$ m above and below the entrainment/detrainment layer. When the mass transfer is

switched off, gravity waves are emitted again in analogy to the process described above (with opposing sign of the vertical wind signal).

3.3.3 | Problems of handling local mass sources in ICON

With the key properties of the dynamical response from the COSMO simulation in mind, we performed the dry mass lifting experiment with the ICON model.

When the OP4DD configuration of the dynamical core is used, the evolving simulated flow pattern is clearly distorted (Figure 5a). Instead of continuous divergence (convergence) around the local mass source (sink) introduced by HYMACS, a convergent (divergent) flow pattern evolves in the detrainment (entrainment) layer. By contrast, the adjacent layers show the expected flow pattern which results in a strong vertical wind shear. Due to continuity, the horizontal inflow in combination with the local mass source at the top of the convective cell is compensated by an enforced vertical outflow imposing a strong vertical wind signal (Figure 5b). The same issue with opposing sign (i.e., horizontal outflow and enforced vertical inflow) is valid at the local mass sink.

The reason for this unphysical dynamical response can be found in the divergence damping term acting as a numerical filter in Equation (10). The actual problem is that the vertical divergence, i.e., the $\partial w/\partial z$ term, is explicitly taken into account for the damping of v_n. Since the local mass sources/sinks introduced by HYMACS force a three-dimensional divergence pattern where the apportionment between horizontal and vertical divergence is a function of the atmospheric stratification (Kuell *et al.* (2007); their figure 3), the vertical wind divergence contributes strongly to the numerical filtering of v_n. In contrast
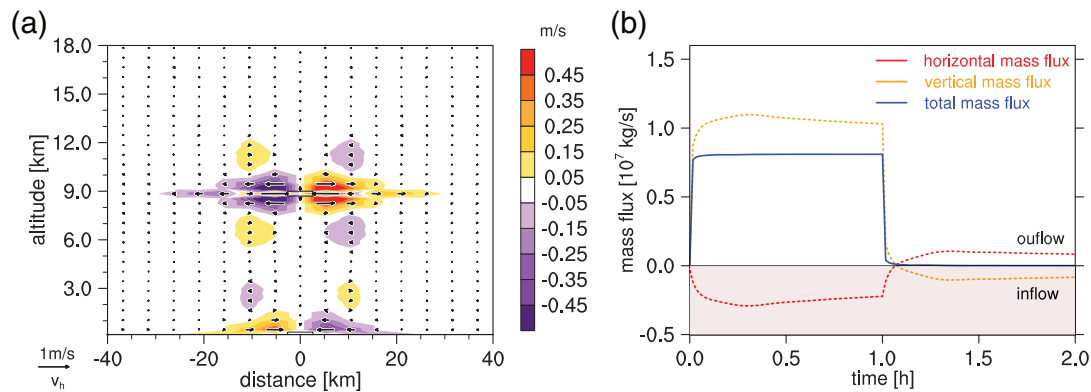
FIGURE 5   Results of the ICON simulation with operational configuration of the dynamical core. (a) Vertical cross-section of the u-wind through the idealized convective cell in zonal direction after 30 min of mass transport in analogy to Figure 4a. Note that every second wind vector in the zonal direction is interpolated due to the ICON's triangular grid. (b) Time series of mass flux across the lateral boundaries of the grid box where detrainment takes place. By convention, outflow (inflow), i.e., mass flux divergence (convergence), occurs for positive (negative) mass flux values

to this, there is no equivalent damping term for the vertical wind. Thus, as the divergence damping term can be interpreted as a hyperviscosity for the horizontal wind, the expected horizontal outflow is *overdamped* in the entrainment layer, causing a convergent horizontal wind field and an unexpected strong vertical wind response.

The problem can be avoided either by foregoing the application of such a numerical filter or by using a modified filter which is compatible with the flow response evoked by HYMACS. While the former is often not a promising approach in numerical models, the latter requires a careful consideration of the architecture of the dynamical core and the closely related grid geometry used in a model.

In the regional model COSMO, numerical stability is achieved by a time-split numerical scheme where a distinction between slow and fast processes is made. In addition to the application of off-centring in the implicit vertical scheme, divergence damping is used to reduce the presence of acoustic waves in the simulations and to stabilize further the time integration (Baldauf, 2010). As an alternative to the operational *anisotropic* divergence damping, an optional *isotropic* divergence damping may be used in COSMO (Baldauf, 2013). Hence, the use of the latter filter is a suitable method for achieving both the guarantee of numerical stability and the compatibility with local mass sources due to the introduction of appropriate damping terms in the vertical wind equation. By contrast, the primary task of the divergence damping in ICON is to reduce inherent problems related to the triangular grid geometry. Consequently, this issue has to be revisited in the following section in order to seek a revised numerical filter which is also compatible with HYMACS.

3.4 | The checkerboard problem and its mitigation in ICON

As already indicated, the triangular grid geometry used in ICON has the drawback of suffering from spurious noise in the divergence field. This issue has already been noticed during the development of the hydrostatic dynamical core in ICON (Wan, 2009) and was discussed in several studies regarding consistent discretizations on triangular C-grids (e.g., Danilov 2010;Gassmann 2011; Wolfram and Fringer 2013). As pointed out by Staniforth and Thuburn (2012), the checkerboard pattern in the divergence field is an undesired computational mode which arises when the numerical discretization of terms in the equation system violates the constraints imposed by their continuous analogue. As a full description of the discretization problem is beyond the scope of this paper, we focus on seeking an approach which mitigates the related checkerboard noise and only briefly summarize the fundamental principles described in Gassmann (2011).

While the triangular grid used in ICON allows for straightforward nesting, the representation of the horizontal wind vector $\mathbf{v}_h$ (and any other vector as well as spatial differential operations) in a trivariate coordinate system has its drawback. Using C-grid staggering as shown in Figure 1, three basis vectors are used to span the two-dimensional space for representing $\mathbf{v}_h$ in terms of $v_{n,i}$ with $i \in \{1, 2, 3\}$. Thus, the vector representation is overspecified, which results in a linear dependency of the face-normal wind components $v_{n,i}$. The associated constraints have to be fulfilled not only in continuous space, but also by its discrete counterpart. Unfortunately, as shown in detail by Gassmann (2011), the imposed constraint cannot be realized on a triangular C-grid.

Even the averaging operation performed in the divergence terms of the discretized prognostic model equations (Equation (12)–(13)) do not prevent the emergence of a checkerboard pattern in the divergence field inherent from the grid geometry.

However, the application of fourth-order divergence damping (Equation (20)) in combination with the imposed averaging procedure for the divergence terms contributes to a minimization of numerical dispersion errors and yields a reasonable performance of the dynamical core in idealized tests and real-case operations (e.g., Z15, Crueger *et al.*, 2018, etc.).

Since the operational numerical filter is incompatible with the local, subgrid mass transfer introduced by HYMACS, the central task is to construct a filter which achieves the following demands besides the compatibility with HYMACS:

1. Efficient mitigation of the checkerboard problem, and
2. Equivalent behaviour of the dynamical core with respect to the operational configuration in common benchmark tests

The latter point corresponds to reducing the foot imprint of the grid in the simulation (cf. Section 4).

Following the preceding discussion, a promising modification of the numerical filter may include the omission of the vertical divergence term from the fourth-order divergence damping (cf. Equation (20))

$$F'_{\text{div},4o}(v_n) = -f'_{d,4o}\overline{A}_C^2 \nabla_n \left[\text{div}\left\{\nabla_n(D_h)\right\}\right]. \quad (24)$$

Note that we have to distinguish between the coefficient $f_{d,4o}$ for the operational damping acting on the 3D divergence and $f'_{d,4o}$ for the damping acting on the 2D divergence.

The application of Equation (24) appears reasonable because the actual requirement for the numerical filter stems from the horizontal grid geometry. Therefore, it is expected that a checkerboard pattern in the divergence is still efficiently removed without taking into account the contribution from the vertical wind. Besides, such a divergence damping is a filter configuration which is also used by other dynamical cores like the GFDL Finite Volume Cubed-Sphere Dynamical Core (FV3; Ullrich *et al.*, 2017) or the Community Atmosphere Model 5 (CAM 5; Lauritzen *et al.*, 2012). Otherwise, despite its scale-selective property, gravity waves might be damped too strongly since the 2D- instead of the 3D-divergence enters $F_{d2,\text{new}}$. As pointed out by Skamarock and Klemp (1992) gravity waves are almost non-divergent and hence their amplitude is only marginally affected when the damping is based on the full 3D-divergence. This desirable property

might be lost with our approach and requires special attention.

In order to minimize the effect on gravity waves, the application of a second-order, *isotropic* divergence damping (in contrast to the fourth-order divergence damping) might be a suitable candidate. This approach relies again on the 3D-divergence, but also introduces appropriate damping terms in $F_d(w)$ of the w-equation (Equation (11)):

$$F_{\text{div},2o}(\mathbf{v}) = f_{d,2o}\overline{A_C}\nabla_n\left(D_h + \frac{\partial w}{\partial z}\right), \quad (25)$$

$$F_{\text{div},2o}(w) = f_{d,2o}\overline{A_C}\frac{\partial}{\partial z}\left(D_h + \frac{\partial w}{\partial z}\right). \quad (26)$$

According to Gassmann and Herzog (2007), an isotropic divergence damping disturbs neither the amplitude of gravity waves nor its frequency solution. Note that the implementation of an isotropic divergence damping required the introduction of the $F_{\text{div},2o}(w)$ terms in the implicit scheme used for the solving the vertical wind equation in ICON. Thus, following the solution strategy described in Prill *et al.* (2019), we extended the linear triangular equation system by appropriately discretized terms describing the vertical change in the 3D divergence.

While this numerical filter is used for example in the Nonhydrostatic Icosahedral Atmospheric Model (NICAM; Tomita and Satoh 2004) and is also available in the COSMO model (see above), its effect on the inherent checkerboard pattern might be limited within our framework due to the weaker scale selectivity of a lower-ordered scheme. Thus, in order to take advantage of both filter techniques, we propose to combine the anisotropic fourth-order and the isotropic second-order divergence damping

$$F_{d2,\text{new}} = F'_{\text{div},4o} + F_{\text{div},2o}. \quad (27)$$

In addition to the combined divergence damping as numerical filter (hereinafter NEWCDD), we also tested hyper-diffusion approaches known from the development history of ICON.

In Wan (2009) and Wan *et al.* (2013), the application of the diffusion operator (hereinafter OLDDIFF) for mitigating the checkerboard noise relies on a vector identity of the vector Laplacian which expresses $\nabla^2\mathbf{v}_h$ in terms of the normal gradient of the horizontal divergence D_h and the tangential gradient of the relative vorticity ζ (equations (13) and (14) in Wan *et al.*, 2013). While the Gauss and Stokes theorem are applied for D_h and ζ, respectively, the centred difference approach is used for calculating the gradients.

TABLE 2 Overview of the different filter configurations in ICON's dynamical core including their acronyms

Acronym	Filter configuration
OP4DD	Operational anisotropic fourth-order divergence damping with $f_{d,4o} = 0.004$ (Equation (20))
NEWCDD	Combined anisotropic fourth-order and isotropic second-order divergence damping with $f'_{d,4o} = 0.0017$ and $f_{d,2o} = 0.002$ (Equation (24) and Equation (27))
OLDDIFF	Hyperdiffusion based on the Laplace discretization with $\tau_{rat} = 13.0$
NEWDIFF	Hyperdiffusion based on the Laplace discretization given in Equation (19) with $\tau_{rat} = 20.0$ and using $\nu_{n,3^\star/4^\star}$

Another efficient diffusion operator (hereinafter NEWDIFF) may be constructed by modifying the discretized Laplacian of the operational diffusion operator used in the non-hydrostatic dynamical core (Equation (19)). In order to enhance the effect on $2\Delta x$ noise of the horizontal wind field, $\nu_{n,3}$ and $\nu_{n,4}$ can be reconstructed on the adjacent cell centre position in the edge-normal direction instead of being reconstructed at the respective vertices. Note that the diffusion has to be applied at every dynamical timestep Δt_{dyn} instead of at every physical timestep Δt_{phy} in order to remove reliably the inherent checkerboard noise.

In the following section, the NEWCDD as well as the diffusional filter configurations OLDDIFF and NEWD-IFF are tested in the Jablonowski test cases. Table 2 gives an overview of the different filter configurations including the associated coefficients $f_{d,4o}$ (Equation (20)), $f'_{d,4o}$ (Equation (24)) and $f_{d,2o}$ (Equation (25)). The hyper-diffusion coefficients k_4 are expressed in terms of an "e-folding time to timestep" ratio τ_{rat} where higher values of $\tau_{rat} > 1$ (i.e., weaker diffusivity) are chosen than in Wan et al. (2013) due to the above-mentioned averaging of the mass and energy flux divergence terms in the equation system ICON's non-hydrostatic dynamical core. However, the focus of the subsequent work lies on the evaluation of the NEWCDD configuration as this numerical filter proves to outperform the two diffusion filters.

4 | JABLONOWSKI–WILLIAMSON TEST CASES

Nowadays, the so-called Jablonowski-Williamson (JW) test cases (Jablonowski and Williamson, 2006) represent a deterministic standard test for dynamical cores and have been widely applied in the modelling community, for example, during the Dynamical Core Model Intercomparison Project (DCMIP; Ullrich et al., 2017). The JW test consist of two parts, both starting with a near-surface meridional temperature gradient of 80 K between the Poles and the Equator. Despite the strong baroclinicity resembling a wintertime atmosphere, the basic state is in hydrostatic and geostrophic balance and no baroclinic disturbances or waves should appear.

The first part, the steady-state JW test, is designed to reveal any imprint of numerical discretization errors. While only dynamical cores whose formulation is based on spherical harmonics or which use latitude–longitude grids are able to maintain the initial state as implied by the balanced state, an irregular grid as used in ICON with the above-mentioned discretization problems may induce disturbances. These disturbances are then prone to trigger baroclinic waves.

The second part, the baroclinic wave JW test, intends to show the diffusivity properties of the dynamical core. By imposing a Gaussian-shaped wind perturbation in the midlatitudes of the Northern Hemisphere, the development of a baroclinic wave train is triggered. The involved cyclones typically start to deepen rapidly after about 7 to 10 days.

The following results are obtained from simulations using a R02B07 grid which corresponds to a grid spacing of $\Delta x_{ICON} \simeq 20$ km (Equation (9)).

4.1 | Steady-state test

The simulations of the steady-state JW tests obtained with the different configurations of the dynamical core as listed in Table 2 can be evaluated in terms of the L2-error of surface pressure. This norm quantifies the global averaged deviation of the surface pressure p_{sfc} from the (balanced) initial state $p_{sfc}(t_0)$ and is therefore a comprehensive metric for evaluation. Following Lauritzen et al. (2012), the initial state is considered to be broken when the L2-error exceeds 0.5 hPa.

As is clearly visible from Figure 6, the configurations which make use of the divergence damping as a numerical filter outperform the simulations where the diffusion is used to mitigate the checkerboard problem. While the initial state is maintained for nearly 18 days with the operational configuration, the above-mentioned threshold is already reached after 8 and 9 days with the NEWDIFF and OLDDIFF simulation, respectively.

The reason for this behaviour may be explained as colon. As any violation of the constraint resulting from the grid geometry manifests itself in a checkerboard pattern of
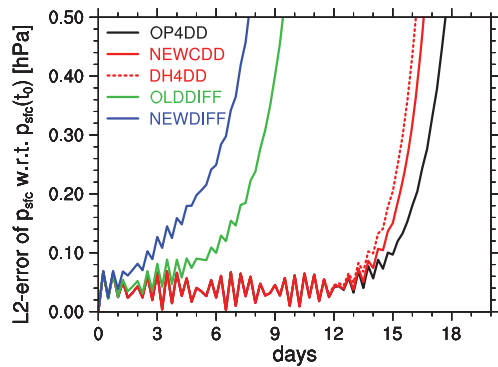
FIGURE 6 Time series of the L2-error of surface pressure for different numerical filter configurations used in ICON's dynamical core in the JW steady-state test. The DH4DD configuration is similar to NEWCDD unless the isotropic second-order divergence damping is switched off (i.e., $f_{d,2o} = 0.0$) in order to demonstrate its effect. Table 2 gives all other acronyms

the horizontal divergence, the usefulness of a divergence damping is quite obvious. The smoothing property of the diffusion operator may also yield a reduction of the inherent small-scale noise in the horizontal wind field, but its mitigation is only a by-product. This problem has already been mentioned by Wan *et al.* (2013), who note that the application of the diffusion as a suitable numerical filter requires relatively large values for the diffusion coefficient k_4. Thus, while the growth of small-scale noise is reliably suppressed, there is the danger of overdamping small-scale meaningful dynamical features.

Besides, the discretitized vector Laplacian of both diffusion operators OLDDIFF and NEWDIFF suffer from additional discretization errors whenever the triangular cells are distorted (Wan 2009; Z15). In the steady-state JW tests, this becomes noticeable since the disturbances develop most likely near the edges of the native icosahedron (not shown) where the distortion is largest despite the spring dynamics optimization (Tomita *et al.*, 2001).

By contrast, the maintenance of the initial state is only reduced by about one day with the NEWCDD configuration. Although the modified fourth-order divergence damping provides the major contribution to reducing the grid imprint on the dynamics as revealed by a sensitivity test with deactivated isotropic second-order divergence damping (DH4DD), the combination of both filter techniques appears rewarding. This is related to the neutral impact of the isotropic second-order divergence damping on gravity waves stated in Section 3.4 which comes along with a slightly slower temporal growth of the L2-error of p_{sfc} (cf. the solid and the dashed red curves in Figure 6).

As a key finding of the steady-state JW test, it is found that the operational OP4DD and NEWCDD configurations are by far superior to diffusion filters. Subsequently presented results from the mass lifting experiments

(performed on a planar grid) are therefore only shown for comparison purposes and for highlighting the usefulness of the NEWCDD configuration.

4.2 | Baroclinic wave test

The obtained results can be further confirmed with the help of the baroclinic wave test. Figure 7 displays the surface pressure and the relative vorticity at 850 hPa after 9 days (a–d) and 11 days (e–h) simulated with the OP4DD and NEWCDD configuration of ICON's dynamical core. After 9 days, the baroclinic wave train is well developed and the leading cyclone has already experienced an explosive cyclogenesis (i.e., a deepening rate of 1 hPa·hr^{-1} over the previous 24 hr). Besides, the leftmost cyclone is already well developed and an additional cyclone development to the east of the major cyclone (downstream development) is detectable. At this stage, the simulation results are practically indistinguishable since the surface pressure difference between the two simulations is below 0.5 hPa everywhere and since the vorticity filaments look very similar.

Two days later, the simulations are still hard to distinguish. The difference in surface pressure seldom exceeds 1 hPa and the vorticity structure keeps general agreement. The most apparent, but rather small, systematical discrepancy can be found near 52°N, 125.5°W along the cold front of the mature low. Here, a secondary cyclone with a central pressure of 987.4 hPa is present in the simulation with the operational ICON set-up. Although present, this low is slightly weaker ($\sim$ 2.5 hPa) and displaced to the southwest with the NEWCDD configuration.

Nevertheless, the simulations diverge only slowly from each other and remain comparable for a long time as the L2-error of the NEWCDD simulation (taking the simulation with the OP4DD configuration as a reference) is below 1 hPa until day 15 (not shown). By contrast, the simulation results obtained with the OLDDIFF and NEWDIFF configurations start to diverge noticeably earlier and stronger from the reference simulation. After 9 days, the pressure differences are larger than 5 hPa in some parts of the baroclinic wave and the cyclones are spatially displaced with respect to the reference simulation (not shown). As stated in Z15, this is probably a side-effect of increased grid imprinting on the simulation.

4.3 | Remarks on the convergence of the solution

The performance of the NEWCDD configuration in comparison to the operational configuration (OP4DD) is further evaluated by checking the convergence property of
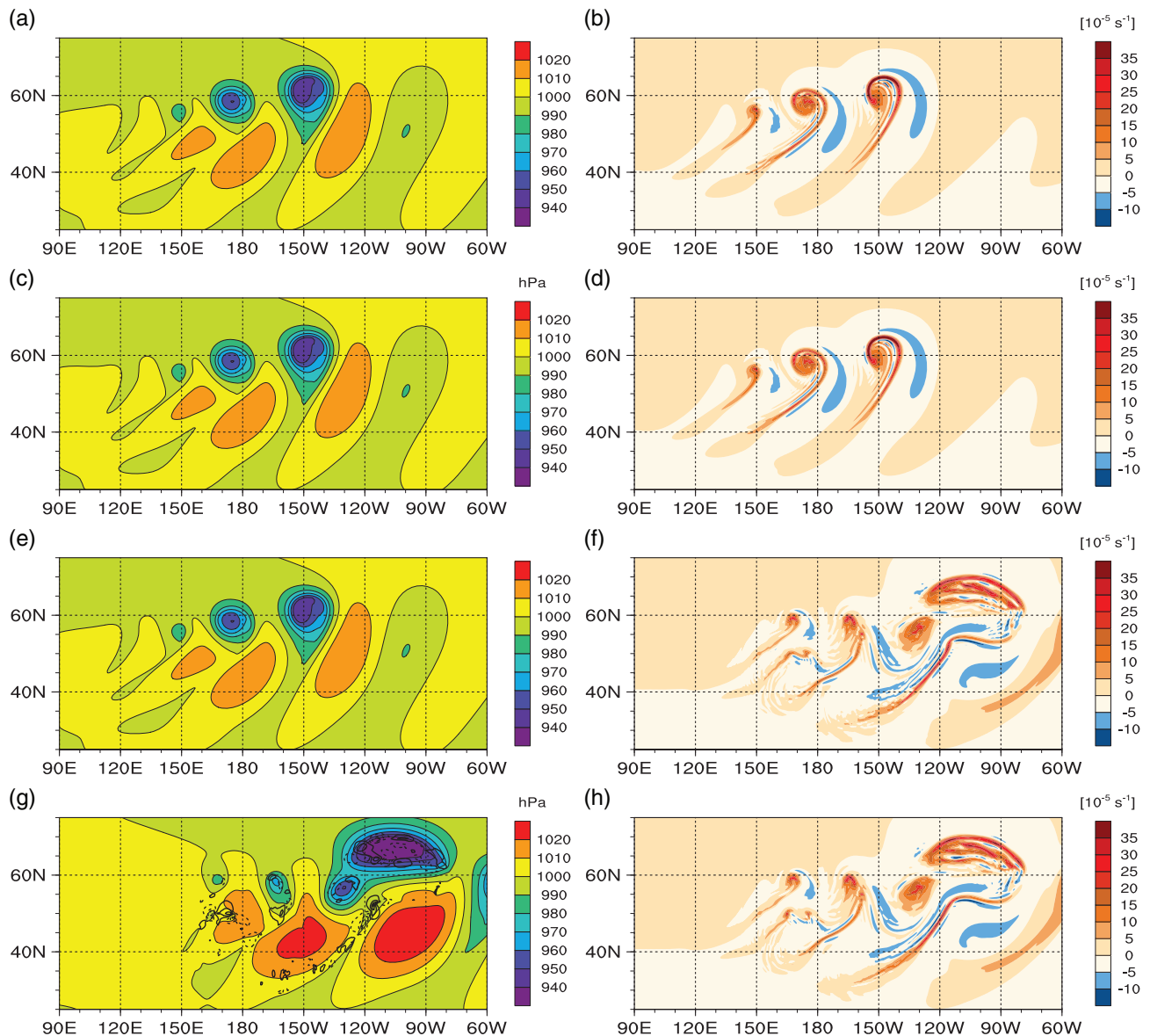
FIGURE 7   (a, c, e, g) Surface pressure (colour shading) and (b, d, f, h) relative vorticity (colour shading) at 850 hPa after (a–d) 9 days and (e–h) 11 days of simulation. The results obtained with the operational configuration of the dynamical core (OP4DD configuration) are displayed in (a, b) and (e, f). The results obtained with the NEWCDD configuration are shown in (c, d) and (g, h), along with the surface pressure difference with respect to the OP4DD configuration as a reference (black contours every 0.5 hPa), with dashed (solid) contour lines for negative (positive) differences, i.e. surface pressure is lower (higher) than in the reference simulation. Note that the difference in surface pressure is still below 0.5 hPa everywhere after 9 days with the NEWCDD configuration

the solution in the JW tests with increasing grid spacing. Additional steady-state tests with varying grid spacing from 160 km (R02B04) to 20 km (R02B07) show a similar convergence property as the reference simulations described in Z15, although the duration of maintaining the geostrophic balanced state increases slightly slower for higher resolutions with the NEWCDD configuration (not shown). Although this behaviour lacks an intuitive explanation, it is probably of minor relevance.

The latter can be confirmed by the convergence of the solution in the baroclinic wave tests with our proposed

numerical filter. The evolution of the baroclinic wave train with different grid spacings (R02B04 up to R02B07) can be considered in terms of the relative vorticity on 850 hPa (Figure 8b,d,f). While the vorticity structure gets smoother with coarser grid spacing, a phase lag is detectable for the left and middle cyclones in the R02B04 simulation. This phase lag is not only an undesired feature of the NEWCDD configuration, but is also present with the OP4DD configuration (Figure 3 in Z15). As revealed by minimizing the L2-error of surface pressure with respect to the R02B07 simulation via zonal shifting, the phase lag is about 5°

with both configurations which is in accordance with the results described in Z15. Inspection of the surface pressure difference $|\Delta p_{sfc}|$ between the simulations obtained with the NEWCDD and the OP4DD configurations reveals that the deviations remain minor for all tested grid spacings. The regions in the R02B04 simulation where $|\Delta p_{sfc}|$ exceeds 0.5 hPa are located north of the middle and right cyclones and hence do not affect the phase lag evaluation metric.

5 | MASS LIFTING EXPERIMENTS WITH ICON'S REVISED NUMERICAL FILTER

In the following section, the mass lifting experiment as described in Section 3.3 is repeated with the revised numerical filter. In addition to the *standard test*, where the mass transfer is switched on instantaneously for 1 hr in the central grid column, some modifications of the experimental design are examined analogous to the test series in Kuell *et al.* (2007). All these experiments are conducted in order to approve the compatibility between the cumulus parametrization scheme HYMACS and the model's dynamical core.

5.1 | The standard test

5.1.1 | Key features of the ICON simulation

The results of the standard test with ICON are summarized in Figure 9. The plots may be compared with the results of the COSMO reference simulation (Figure 4) and can be opposed to the simulation characteristics obtained with the operational numerical filter (Figure 5).

In contrast to the distorted dynamical response evolving with the OP4DD configuration, a continuous divergent (convergent) flow pattern is visible around the mass source (sink) with the NEWCDD configuration after 30 min of continued mass transfer. The horizontal divergence (convergence) is strongest in the layer where the mass transfer between HYMACS and the grid-scale occurs while the outflow (inflow) pattern extends to about 1,000 m in vertical direction (Figure 9a). The generation of (grid-scale) gravity waves as a response to the imposed perturbation of the hydrostatic balance after switching on/off the mass transfer is also comparable to the COSMO reference simulation. While the amplitude of the vertical wind reaches a value of 0.005 m·s^{-1} up to a distance of 20 km, the oscillation with nearly identical cycle frequencies fades away again after about 30 min (Figure 9b,c).

Despite the apparant resemblance of the dynamical response between the COSMO reference and the ICON simulation with the revised numerical filter, there are also some differences which deserve further consideration.

At first, the amplitude of the *central* vertical wind oscillation between the entrainment and detrainment layer is somehow weaker with ICON (Figure 9c). While the vertical wind reaches a value of 0.075 m·s^{-1} about 10 min after switching on the mass transfer in COSMO, the maximum value of w is only 0.052 m·s^{-1} in ICON. Further tests reveal that the local grid-scale vertical wind signal is sensitive to the strength of the vertical wind diffusion and to the configuration of the divergence damping in both models. For example, a smaller value of the divergence damping coefficient $f'_{d,4o}$ may enhance the localized w-maximum in ICON but, as discussed in Section 5.3, this would also evoke stronger checkerboard noise. However, despite the weaker *local* oscillation of w, the vertical wind signal in the vicinity of the convective grid column is very similar in ICON and COSMO. This confirms that the emitted gravity waves which play a crucial role in adjusting the environment are retained.

Secondly, an albeit weak, but clearly visible, cross-circulation develops around the entrainment and detrainment layer in the ICON simulation. About 2,000 m above and below the mass source layer, the flow pattern is slightly convergent as opposed to the strong divergence between. Closer investigation of Figure 4a shows that this cross-circulation is also present in the COSMO simulation, even though it is weaker. As further tests with COSMO reveal, the formation of the cross-circulation is sensitive to the strength of the diffusion applied on the horizontal wind. With smaller diffusion coefficients, this pattern may attain a similar amplitude as in the ICON simulation (not shown). Hence, the differences between the dynamical response to the mass transfer with HYMACS can be explained by the different numerical filters used in the two models.

5.1.2 | Analysis of kinetic energy spectra

In order to get further insight into the dynamical response evoked by HYMACS, we additionally calculated spectra of the horizontal kinetic energy for the mass lifting experiments. Again, the results obtained with the COSMO model can be considered as a reference since its quadrilateral grid does not suffer from the above-mentioned checkerboard problem related to a triangular grid.

While the computation of the one-dimensional wave number spectra of kinetic energy from zonal and meridional wind components given on a regular grid like in COSMO is straightforward (Errico, 1985; Bierdel *et al.*,
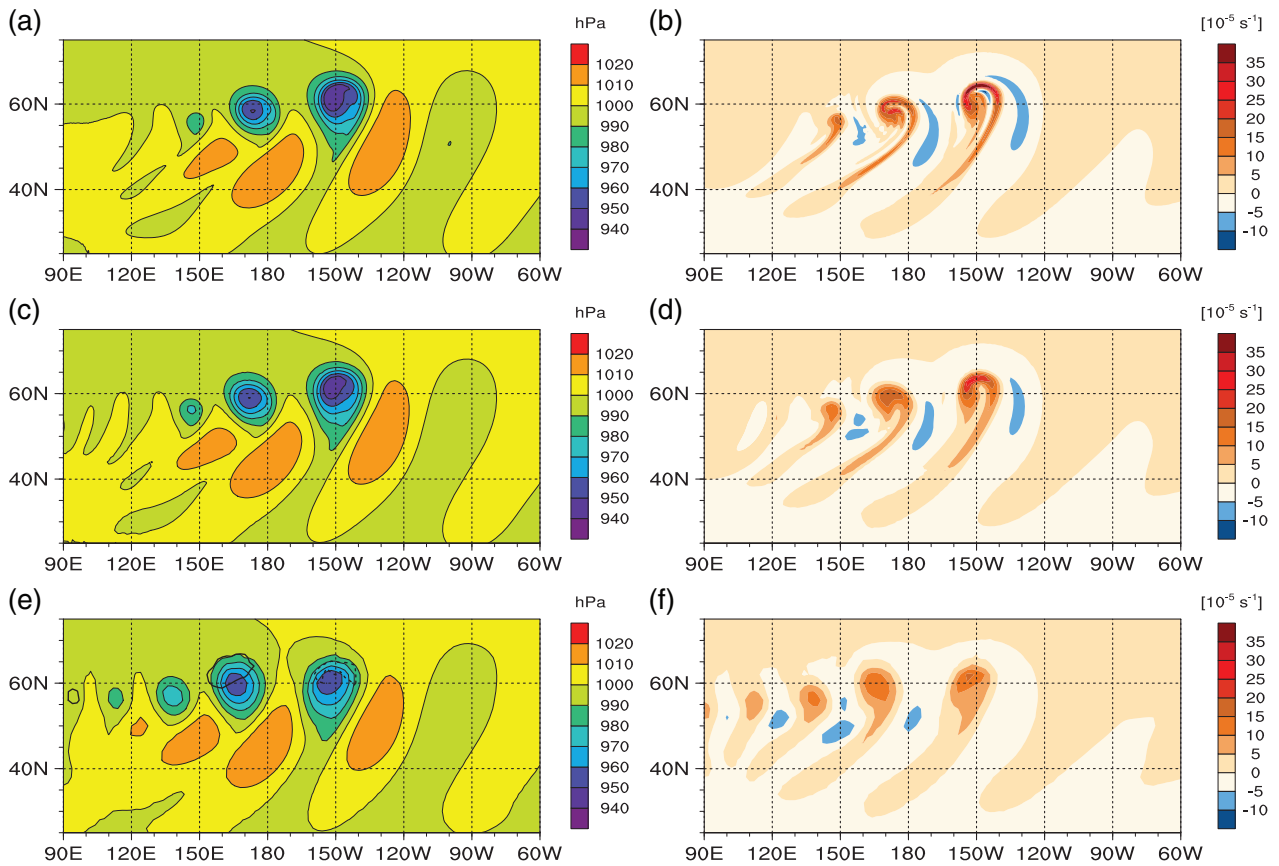
FIGURE 8 As Figure 7, but for simulations with the NEWCDD configuration at different spatial resolutions. The used model grids are (a, b) R02B06, (c, d) R02B05 and (e, f) R02B04 which correspond to grid spacings of 40, 80 and 160 km, respectively
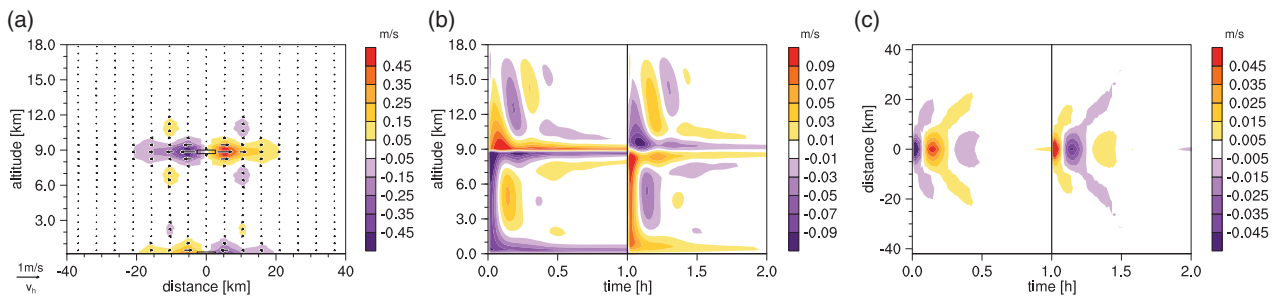

FIGURE 9 Results of the mass lifting experiment (standard test) obtained with ICON using the NEWCDD configuration. The overall dynamical response can be compared with the results of the COSMO reference simulation (Figure 4). The vertical cross-section through the convective column (a) can be compared to the results obatined with ICON's operational numerical filter (Figure 5a)

2012), interpolation is necessary for triangular meshes as a preprocessing step. In addition to the sensitivity of the results with respect to the interpolation method, an *priori* estimation of the *spectral resolution* of ICON's grid $\Delta x'_{\text{ICON}}$ is required. When the grid spacing of the regular target grid is too small, alias effects may distort the spectrum due to accumulation of energy near the Nyquist limit. Following Dipankar *et al.* (2015), we make use of

$$\Delta x'_{\text{ICON}} = 0.87 l_{\text{E}} \tag{28}$$

in order to preclude alias effects due to accumulation of energy near the Nyquist limit. Thus, the estimator of spectral resolution is slightly coarser than the cell-area-based definition (Equation (9)) which is given on a planar grid by

$$\Delta x_{\text{ICON}} = (3^{1/4} l_{\text{E}})/2 \approx 0.66 l_{\text{E}} < \Delta x'_{\text{ICON}}. \tag{29}$$

However, the latter definition would mean that the degree of freedom per grid cell for velocity components on the regular grid is less than on the triangular grid.
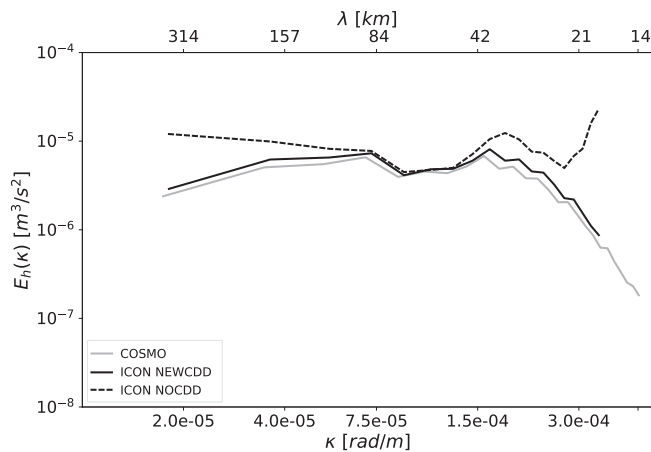
FIGURE 10 Kinetic energy spectra obtained 30 min after switching on the mass transfer with HYMACS. Note that the spectrum of the COSMO reference simulation inhibits shorter waves due to finer spectral resolution with the quadrilateral grid than the triangular grid (see text for further details)

FIGURE 11 As Figure 10, but kinetic energy spectra obtained at the end of the forcing phase (solid curves) and 30 min after switching off the mass transfer (dotted curves)

The regular target grid comprising 39 grid points in each horizontal direction is centred at the convective grid column. The wind components at each grid point are then obtained by a RBF vector reconstruction of the horizontal wind vector using a nine-point stencil with a Gaussian kernel (Rípodas *et al.*, 2009). Since the (horizontal) dynamical response is strongest in the layers around the mass source and sink, the kinetic energy spectra are computed for the detrainment layer and the two adjacent layers in the following analysis (model layers 30–32).

The kinetic energy spectra after 30 min of continued mass transport for the simulations with ICON (NEWCDD configuration) and COSMO are displayed in Figure 10. It can be seen that the shape of the energy spectra is very similar in the two models. A maximum of the spectral energy at a wavelength of 40 km shows that the outflow now extends over several grid boxes in the vicinity of the convective grid column, while there is a strong decrease at shorter wavelengths. The latter confirms the effect of the numerical filter in ICON which efficiently suppresses checkerboard noise. By contrast, the black line shows the energy spectrum for an ICON simulation *without any* divergence damping (NOCDD). Here, a clear bump near the shortest resolvable wavelength $\lambda = 2\Delta x'_{ICON} \approx 18$ km is visible, which shows that the dynamical response is spoiled by numerical noise.

At the end of the forcing phase, that is after 60 min of continued mass transfer by HYMACS, the energy spectra from COSMO and ICON are still similar (the solid lines in Figure 11). The maximum of the spectral kinetic energy is now found at wavelengths of around 80 km, while the energy falls off quickly for shorter wavelengths. However,
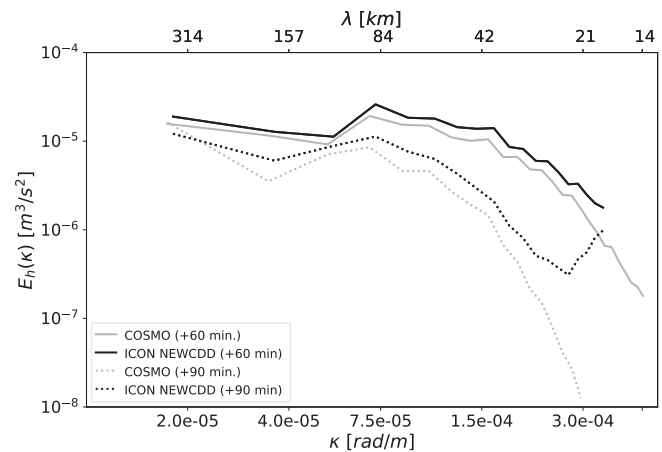
near the shortest resolvable wavelength, the spectrum becomes slightly flatter in the ICON (NEWCDD) simulation, which is an indicator for the presence of small-scale noise. Although the weak kink in the kinetic energy spectrum is an undesired feature, its significance is questionable due to its small magnitude compared to the overall dynamical response. It is noted that the kink also appears at the end of the forcing phase (i.e., after 1 hr of mass lifting) in the simulations with the diffusion operators as a numerical filter (not shown).

The inherent checkerboard problem of ICON becomes more pronounced after switching off the forced mass exchange by HYMACS. Following the emission of gravity waves due to the abrupt end of the mass transfer, the induced flow pattern starts to fade away. Without any forcing, dissipation processes lead to a temporal reduction of the kinetic energy within the idealized atmosphere.

As can be seen form the energy spectrum of the COSMO simulation 30 min after switching off the mass transfer (the dashed lines in Figure 11), the decrease in spectral kinetic energy is strongest for the shortest waves. This is related to the numerical diffusion in conjunction with the isotropic divergence damping which dissipate the kinetic energy most effectively for the shortest wavelengths. While this is common for numerical filters which reduce the effective resolution of any numerical model to the range between $6\Delta x$ and $10\Delta x$ (Skamarock, 2011), the situation is different near the shortest resolvable waves in ICON. Here, a bump in the spectral energy indicates the stronger emergence of checkerboard noise in the dissipation phase. Inspection of the temporal evolution of the kinetic energy spectra reveals that the spectral energy decreases for all wave numbers after switching off the mass transfer. Even though this decline is similar in COSMO and
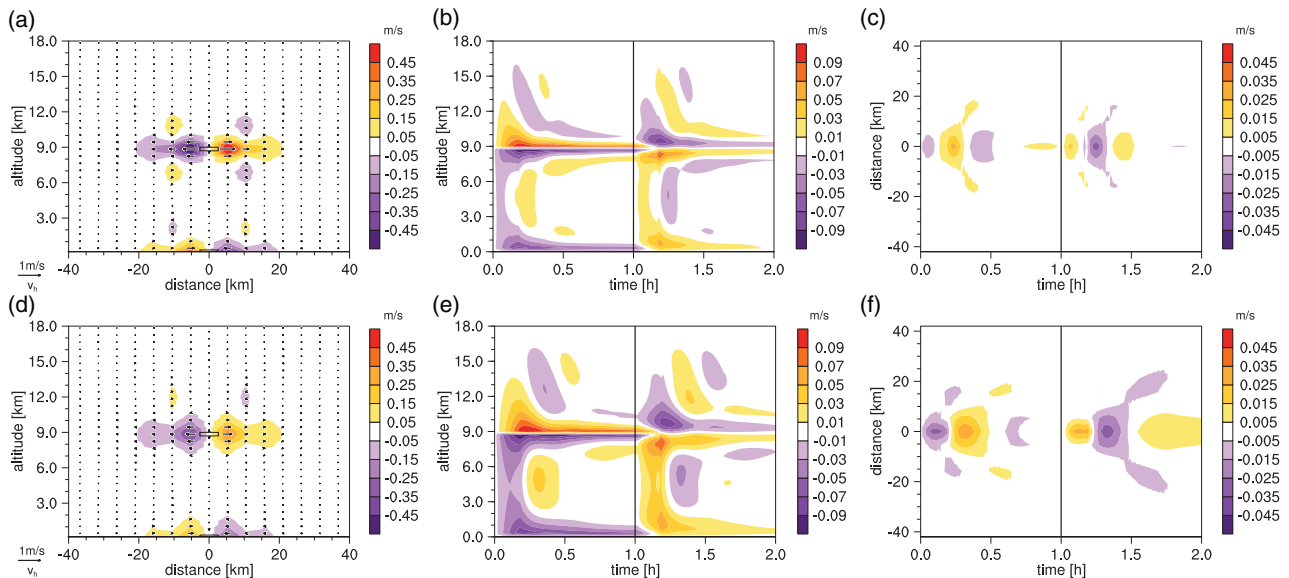
FIGURE 12 As Figure 9, but for varying stratification of the background atmosphere and temporal evolution of the subgrid mass transport. (a–c) are for a lapse rate of 4 K·km^{-1}, and (d–f) for a lapse rate of 8 K·km^{-1}

ICON up to a wavelength of $3\Delta x'_{\text{ICON}}$, it is much weaker for the shortest resolvable waves in ICON (not shown), thus leading to a temporal growth of the bump. Owing to the highly idealized experimental set-up, the relevance of this problem is questionable in real-case applications (Section 5.3).

5.2 | Further mass lifting experiments

Following the thread of the test series in Kuell *et al.* (2007) and ensuring a proper dynamical response under various situations, we performed further mass lifting experiments by varying the atmospheric stratification and the grid spacing. Again, the results can be compared with corresponding COSMO reference simulations.

In addition to the above-mentioned changes in the experimental design, a simple temporal evolution is imposed in the subsequent tests. The mass flux as well as the height of the detrainment layer undergo a linear increase during the first 10 min, thus imitating a simple life cycle of a convective cell. The temporal evolution does not significantly affect the stationary flow pattern, but modifies the gravity wave emission. In agreement with Chagnon and Bannon (2005), the gradual increase of the mass flux weakens the amplitude of the gravity wave signal, whereas it is restrengthened with the vertical growth of the cell. It is notable that the current version of the cloud model of HYMACS may represent such a life cycle since the turbulent mixing is decreased with increasing age of a convective cell as a simplified mechanism for convective memory (Kuell and Bott, 2011). Although this feature is

not included with a deactivated cloud model, its dynamical response is addressed in the idealized test suite at hand.

5.2.1 | Dependence on atmospheric stratification

The properties of the emitted gravity waves depend on the stratification of the background atmosphere which can be expressed in terms of the Brunt–Väisälä frequency N. While the frequency of the associated oscillations is proportional to N, their amplitude is proportional to $1/N$ (e.g., Bretherton and Smolarkiewicz 1989; Holton and Hakim 2013). Thus, for a less stable atmospheric stratification (smaller N), the frequency of the vertical wind oscillation should be reduced and its amplitude should be stronger.

The simulation results obtained with a lapse rate of 4 and 8 K·km^{-1} in Figure 12 confirm this dependence. It can be seen that the amplitude of the oscillation is stronger and that the frequency is reduced for the less stable atmospheric stratification, as expected. The temporal distance between the minimum and maximum of w is about 11 min for a lapse rate of 4 K·km^{-1} and 14 min for 8 K·km^{-1}, respectively. This corresponds to an increased cycle time of about 25%, akin to the results obtained with the COSMO model.

It is also confirmed that the quasi-steady divergence flow pattern around the local mass source and sink is shifting from the horizontal to the vertical with a steeper vertical gradient in temperature of the background atmosphere (compare Figure 12a,b with d,e). The shift to a stronger signal in the vertical flow field can also be readily
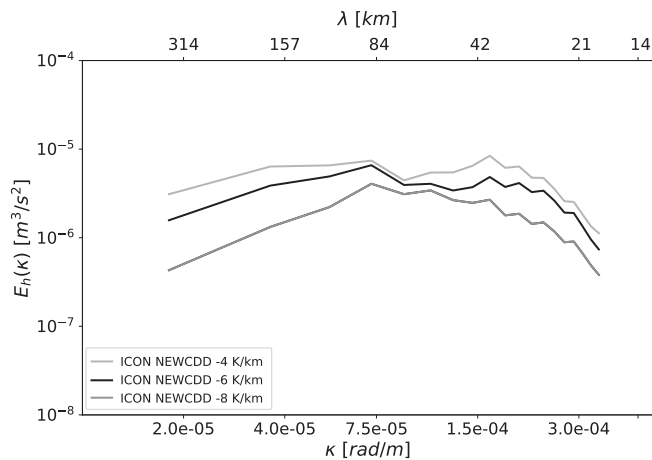
FIGURE 13 As Figure 10, but kinetic energy spectra for ICON simulations (using the NEWCDD configuration) after 30 min of continued mass transport with variable stratification of the background atmosphere

seen in the horizontal kinetic energy spectra in Figure 13 with the weakest energy for a lapse rate of 8 K·km^{-1}. Note that the overall weaker gravity wave signal seen in Figure 12 compared to Figure 9 can be related to the linear increase (decrease) of the subgrid mass flux as opposed to the instantaneous (de-)activation in the standard test.

5.2.2 | Independence of the grid spacing

As pointed out by Kuell *et al.* (2007), an important issue for HYMACS is the independence of the evolving dynamical flow pattern from the grid spacing used in the model. In analogy to their tests with a quadratic 56 × 56 km cluster of convective cells in COSMO, we performed experiments with an equal-sized triangular cluster (i.e., with an edge length of 84 km) in ICON. By three successive bisection steps starting with a coarse triangular grid of edge length $l_E = 42$ km ($\Delta x_{ICON} \approx 28$ km), four different simulations can be compared. Since the cluster area is constant in all experiments in order to ensure a constant total mass flux, the cluster consists of 4, 16, 64, 256 cells with an edge length of 42, 21, 10.5 and 5.25 km, respectively.

In agreement with the results obtained with COSMO, the large-scale flow pattern as a response to the subgrid mass transfer looks similar irrespective of the grid spacing. As an example, Figure 14 shows a zonal cross-section of the *u*-wind through the circumcentre of the cluster after 30 min of continuous mass exchange for $\Delta x_{ICON} = 3.5$ km (Figure 14a) and for $\Delta x_{ICON} = 14$ km (Figure 14b). In the higher-resolution simulation, a stronger outflow/inflow appears at the boundaries of the convective cluster because more small-scale structures can be represented on the

grid-scale with a finer resolution of the underlying grid. Thus, in order to confirm that the differences can be attributed to the grid-scale/subgrid-scale limit on a certain grid, we averaged the output fields onto a coarse grid with an edge length of 84 km. The cross-sections of the averaged *u*-wind through the convective cluster are shown for all four simulations in Figure 15. It can be seen that the flow pattern becomes very similar for all simulations except for the simulation with the coarsest grid spacing. With an edge length of 42 km, the flow pattern appears to be slightly stronger with a greater vertical extent of the outflow. Interestingly, the latter finding differs from the results obtained with the COSMO model, where the coarsest resolution run looked smoother than the finer ones (Kuell *et al.*, 2007). However, it is confirmed that the flow pattern evolving due to a given subgrid-scale total mass flux over a fixed area is rather insensitive to the grid spacing.

5.3 | Significance for more realistic applications

The dry mass lifting tests in the previous subsections confirm that a proper dynamical response to a parametrized net mass transport is achieved for various conditions, provided our proposed numerical filter configuration is applied. Nonetheless, our experiments also reveal situations where checkerboard noise becomes more noticeable; these are the dissipation phase subsequent to the continued mass lifting (Figure 11) and lingered forcing in an unconditionally stable background atmosphere with a lapse rate of 4 K·km^{-1} (cf. Section 5.2.1).

The former case is argued to be rather academic since an atmosphere without any forcing (neither small- nor large-scale) is very unlikely with a full physics coupling. Hence, the developing bump in the energy spectrum is expected to be of minor relevance, although its evidence is just concealed by forcings other than convection.

By contrast, the latter case may also be present in real-case applications. The atmosphere is typically conditionally unstable near the source layers of the convective cell (i.e., lapse rate $\gamma > 6$ K · km^{-1}), whereas stably stratified conditions are normally present near the cloud-top level (CTL) where the rising air parcels lose their buoyancy. Given that the organized detrainment at the CTL persists for a longer time, checkerboard noise may become more noticeable as indicated by the growing kink in the energy spectrum in Figure 13 (the light grey curve). [Correction added on 22 June 2020 after first publication: the second sentence in this paragraph has been corrected in this version.]

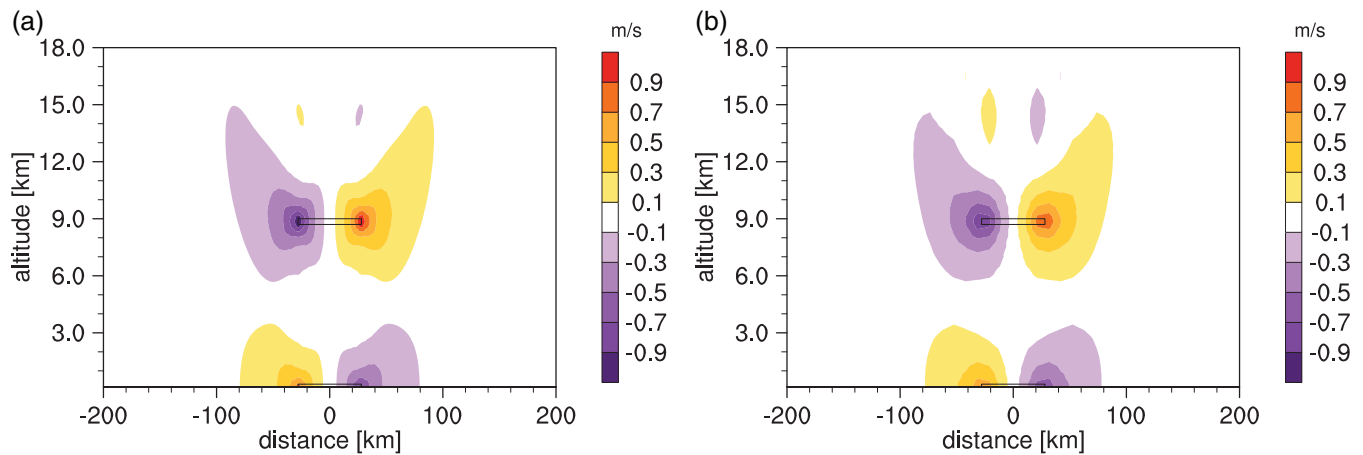Certainly, we note that the assumption of vanishing enthalpy tendencies in our experimental set-up

FIGURE 14   Vertical cross-section of the u-wind through the circumcentre of the convective cluster after 30 min of continued mass transport with HYMACS. (a) Results obtained with an edge length of $l_E = 5.25$ km ($\Delta x_{ICON} = 3.5$ km) of the triangular cells. (b) is as (a), but with $l_E = 21$ km ($\Delta x_{ICON} = 14$ km)

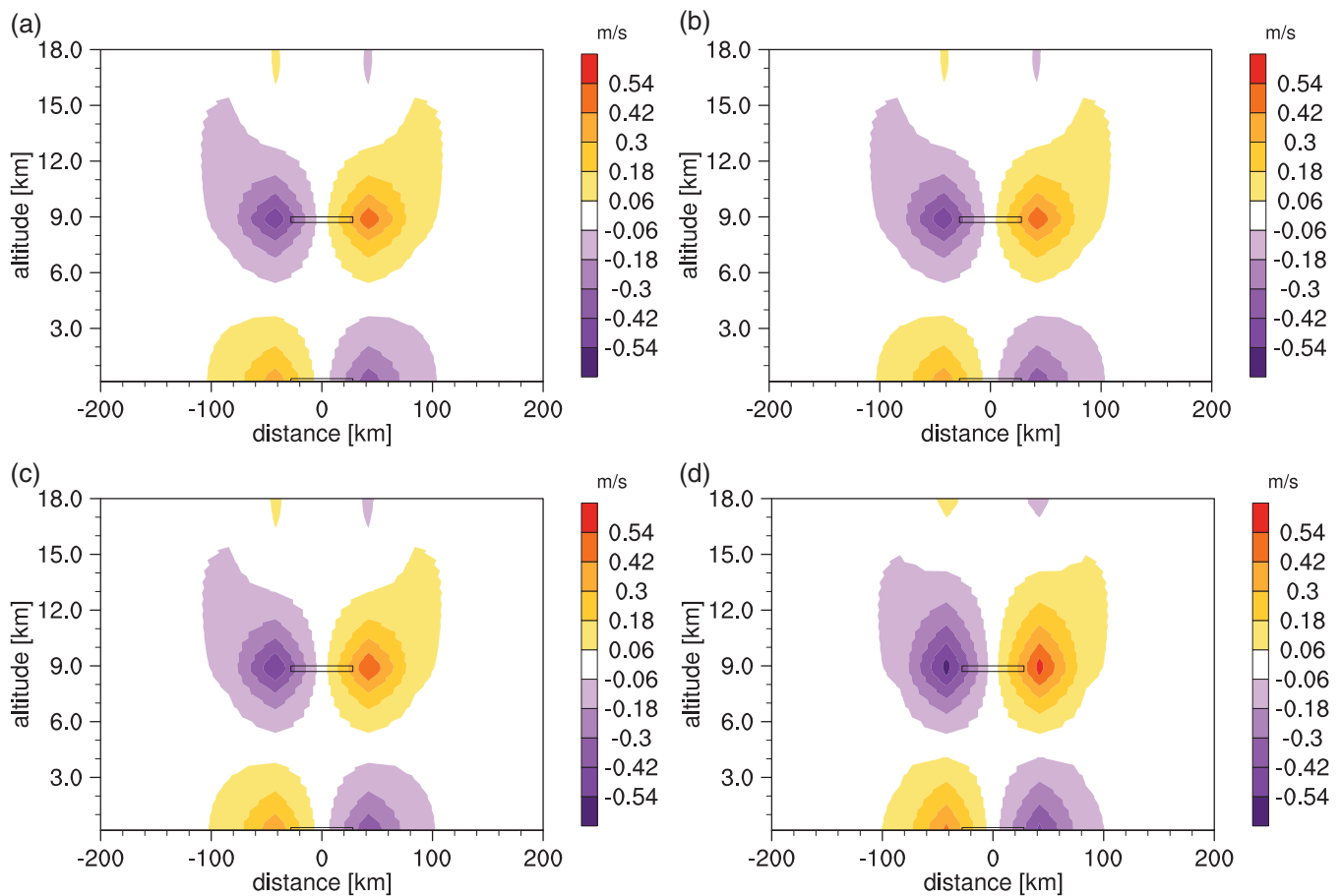**FIGURE 15**   As Figure 14, but u-wind averaged on a coarse grid with $l_{E,coa} = 84$ km for four simulations with different grid spacings. The native triangular edge length l_E of the simulations are (a) 5.25 km , (b) 10.5 km, (c) 21 km and (d) 42 km

(Section 3.3) is a crude simplification near the CTL where the updraught air becomes colder than the environment in real (moist) convective cells. Accordingly, in order to adapt our mass lifting experiment while retaining the

idealized framework with a deactivated cloud model (note the discussion on microphysical effects in Section 6), we perform an additional sensitivity test where the detrained air is colder than the environment by 2 K (hereinafter the
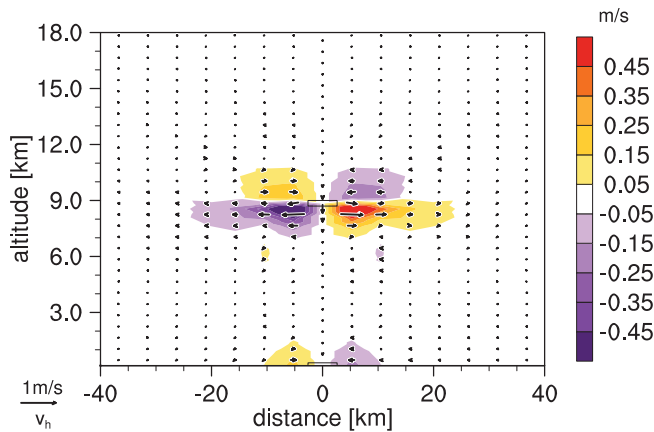
FIGURE 16 As Figure 9a, but for the COLDUP experiment (see text for further details)
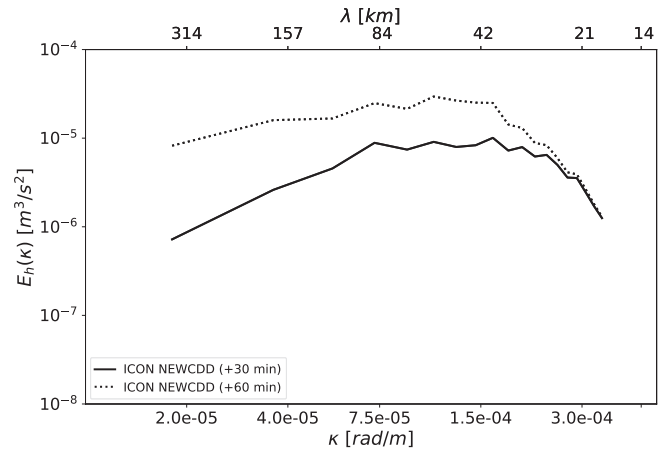

FIGURE 17 Kinetic energy spectra obtained after 30 min (solid curve) and 60 min (dotted curve) of mass transfer in the COLDUP experiment (see text for further details). Note that the spectral analysis was performed for model layers (28–30) underneath the detrainment layer (31) since the horizontal dynamical response is strongest there

COLDUP experiment). For the background atmosphere in this experiment, we initialize a lapse rate of $8\,\mathrm{K}\cdot\mathrm{km}^{-1}$ below 8 km with a gradual transition to a more stable stratification with $4\,\mathrm{K}\cdot\mathrm{km}^{-1}$ underneath the organized detrainment layer. Besides, guided by the mass flux profiles presented in Kuell *et al.* (2007) (their Figure 6) and Kain and Fritsch (1990) (their Figure 5), we pursue mimicking a more realistic set-up by imposing organized entrainment in mid-level layers.

Due to the relatively cold detrained air, strong grid-scale subsidence is triggered underneath the detrainment level (Figure 16). The horizontal divergent outflow is then shifted to lower levels where the atmosphere becomes less stably stratified again which is in accordance with the results presented in Kuell *et al.* (2007) (cf. their Figure 7). Consequently, *no kink* in the kinetic energy spectrum shows up for a continued mass transport over a period of 60 min (Figure 17). Thus, it is concluded that the above-mentioned emergence of checkerboard noise is again less relevant in more realistic set-ups or real-case applications.

Finally, we mention that the configuration of the combined divergence damping in terms of their coefficients $f_{d,2o}$ and $f_{d,4o}'$ should be understood as first guideline values. However, due to its potential degenerative effects on gravity waves, variations of $f_{d,4o}'$ controlling the strength of the fourth-order divergence damping should be chosen with care. Higher values, say $f_{d,4o}' \gtrsim 0.0025$, conceal the occurrence of inherent checkerboard noise, but have the drawback of also noticeably damping emitted gravity waves.

6 | CONCLUSIONS

Representing convection in modern NWP models which operate within the convective grey zone ($\Delta x \sim 1$–10 km)

is challenging due to several different reasons. Among other approaches, the hybrid mass flux convection scheme HYMACS of Kuell *et al.* (2007) enables a stronger coupling with the grid-scale dynamics and therefore its implementation in a unified modelling framework such as ICON appears attractive.

In the first part of the paper, we revisit the principles of the hybrid approach based on the concept of fluid volumes. In contrast to conventional CPS, HYMACS realizes a net mass transport of the convective draughts and passes the environmental subsidence to the explicit (grid-scale) dynamics of the hosting model.

After sketching the revised physics–dynamics coupling of HYMACS in ICON which can be neither isobaric nor isochoric, the incompatibility of the operational numerical filter with local mass sources and sinks is discussed. This incompatibility is related to the anisotropic property of the fourth-order divergence damping where w affects explicitly the horizontal wind field while the vertical wind itself remains unchanged. As a consequence, a distorted dynamical response develops with horizontal convergence (divergence) in the detrainment (entrainment) layer due to the forced three-dimensional outflow (inflow). For continuity reasons, the local mass source (sink) plus the artificial horizontal convergence (divergence) have to be compensated by an increased grid-scale outflow (inflow) in the vertical direction which further spoils the dynamical flow response.

However, the emergence of checkerboard noise in the divergence field inherent from the triangular grid requires a numerical filter in ICON. Thus, we test different filter configurations adapted from the development

history of the new hosting model, which are two diffusion approaches (OLDDIFF and NEWDIFF) and a combination of an isotropic second-order divergence damping with a modified fourth-order divergence damping (NEWCDD). Based on the outlined incompatibility of the operational filter, the contribution from the vertical wind (the $\partial w/\partial z$ term) is omitted in the modified fourth-order divergence damping.

While the NEWCDD configuration yields similar results to the operational set-up, the tested diffusion operators reinforce the grid imprint in the scope of the Jablonowski–Williamson test cases. The reason for this result has already been argued in the literature (e.g., Wan 2009; Wan *et al.*, 2013 and Z15). The mitigation of the checkerboard problem is only a by-product and further discretization errors of the vector Laplacian give rise to (stronger) perturbations near the native icosahedron's edges and pentagon points. Thus, the OLDDIFF and NEWDIFF configurations are less suited for applications on a spherical grid.

The usefulness of a combined divergence damping is further confirmed by idealized dry mass lifting experiments with HYMACS. The dynamical response which includes the emission of gravity waves and a divergent (convergent) flow pattern around local mass sources (sinks) proves to be proper under various situations. Analysis of kinetic energy spectra also reveals that checkerboard noise is efficiently suppressed.

Nonetheless, a net mass transport into stably stratified layers has the potential to generate a more pronounced checkerboard signal in the flow pattern. Although such a process is common near the cloud-top layer of convection cells, its relevance in more realistic applications is presumably minor, as revealed by the COLDUP experiment with organized detrainment of relatively cold air. Also note that the increased potential for small-scale noise with stronger mass fluxes than in our mass lifting experiment may be compensated by thicker upper-level layers in a stretched vertical grid.

In summary, a proper physics–dynamics coupling of HYMACS with ICON is achieved which enables ongoing progress of our CPS in the new hosting model.

For the future, further steps are needed in order to enhance the scale adaptivity of HYMACS. Although the net mass transport results in a better coupling between the grid-scale dynamics and the parametrized convection, high-resolution tests with HYMACS in COSMO do not converge to a *cloud-resolving* behaviour of the model with decreasing subgrid convective mass transport. As argued by Arakawa *et al.* (2011), the missing convergence is related to the assumption that the gridpoint values are used to represent the cloud environment. From Equation (6), it can be seen that this issue is also acute in HYMACS. In order to obtain a smooth transition to an explicit representation of convection, Arakawa and Wu (2013) propose relaxation of the convective transport.

Other issues for further developments of HYMACS are related to the handling of microphysical processes in the parametrized draughts and to the closure assumption. We note that the microphysical effects in HYMACS are rather crudely handled in comparison with the elaborate microphysical package of ICON which is adopted from the COSMO model (Doms *et al.*, 2011). In order to at least reduce this discrepancy and thereby reduce spurious competition between grid-scale and convective precipitation/cloud formation (Wu and Arakawa, 2014), the enhancement of the cloud model may also be conducive. The horizontal mass flux convergence closure used in HYMACS has the advantage of interactively determining the subcloud organized entrainment profiles. By contrast, more commonly used closures based on quantities more closely related to atmospheric instability (Yano *et al.*, 2013 give a review) would require a rather arbitrary predescription of the subcloud mass flux evolution. Thus, further consideration would be necessary if a revised closure is implemented in a future HYMACS version.

From the discussion above, we conclude that further progress in representing moist convection across the convective grey zone with HYMACS can be expected. The ICON model which is designed for applications over various spatial scales constitutes an excellent framework for this aim. Thus, the presented work is considered to be a prerequisite for further steps since a proper dynamical response to local mass sources is fundamental for HYMACS.

ORCID

M. Langguth https://orcid.org/0000-0003-3354-5333
V. Kuell https://orcid.org/0000-0001-6012-1697

REFERENCES

Arakawa, A. (2004) The cumulus parameterization problem: past, present, and future. *Journal of Climate*, 17, 2493–2525.

Arakawa, A. and Schubert, W.H. (1974) Interaction of a cumulus cloud ensemble with the large-scale environment: Part I. *Journal of Atmospheric Sciences*, 31, 674–701.

Arakawa, A. and Wu, C.-M. (2013) A unified representation of deep moist convection in numerical modeling of the atmosphere: Part I. *Journal of the Atmospheric Sciences*, 70, 1977–1992.

Arakawa, A., Jung, J.-H. and Wu, C.-M. (2011) Toward unification of the multiscale modeling of the atmosphere. *Atmospheric Chemistry and Physics*, 11, 3731–3742.

Baldauf, M. (2010) Linear stability analysis of Runge–Kutta-based partial time-splitting schemes for the Euler equations. *Monthly Weather Review*, 138, 4475–4496.

Baldauf, M. (2013). A new fast-waves solver for the Runge–Kutta dynamical core. Technical Report 21, Deutscher Wetterdienst, Offenbach, Germany.

Baldauf, M., Seifert, A., Foerstner, J., Majewski, D. and Raschendorfer, M. (2011) Operational convective-scale numerical weather prediction with the COSMO model: description and sensitivities. *Monthly Weather Review*, 139, 3887–3905.

Bechtold, P., Bazile, E., Guichard, F., Mascard, P. and Richard, E. (2001) A mass flux scheme convection scheme for regional and global models. *Quarterly Journal of the Royal Meteorological Society*, 127, 869–886.

Bechtold, P., Semane, N., Lopez, P., Chaboureau, J.-P., Beljaars, A. and Bormann, N. (2014) Representing equilibrium and nonequilibrium convection in large-scale models. *Journal of the Atmospheric Sciences*, 71, 734–753.

Bengtsson, L., Steinheimer, M., Bechtold, P. and Geleyn, J.-F. (2013) A stochastic parametrization for deep convection using cellular automata. *Quarterly Journal of the Royal Meteorological Society*, 139, 1533–1543.

Betts, A.K. and Miller, M.J. (1993). The Betts–Miller scheme, pp. 107–121 in The Representation of Cumulus Convection in Numerical Models. Emanuel, K.A. (ed.), Springer, Berlin.

Bierdel, L., Friedrichs, P. and Bentzien, S. (2012) Spatial kinetic energy spectra in the convection-permitting limited-area NWP model COSMO-DE. *Meteorologische Zeitschrift*, 21, 245–258.

Bretherton, C.S. and Smolarkiewicz, P.K. (1989) Gravity waves, compensating subsidence and detrainment around cumulus clouds. *Journal of the Atmospheric Sciences*, 46, 740–759.

Bryan, G.H., Wyngaard, J.C. and Fritsch, J.M. (2003) Resolution requirements for the simulation of deep moist convection. *Monthly Weather Review*, 131, 2394–2416.

Chagnon, J.M. and Bannon, P.R. (2005) Adjustment to injections of mass, momentum, and heat in a compressible atmosphere. *Journal of Atmospheric Sciences*, 62, 2749–2769.

Crueger, T., Giorgetta, M.A., Brokopf, R., Esch, M., Fiedler, S., Hohenegger, C., Kornblueh, L., Mauritsen, T., Nam, C., Naumann, A.-K., Peters, K., Rast, S., Roeckner, E., Sakradzija, M., Schmidt, H., Vial, J., Vogel, R. and Stevens, B. (2018) ICON-A, the atmosphere component of the ICON earth system model: II: model evaluation. *Journal of Advances in Modeling Earth Systems*, 10, 1638–1662.

Danilov, S. (2010) On utility of triangular C-grid type discretization for numerical modeling of large-scale ocean flows. *Ocean Dynamics*, 60, 1361–1369.

Deng, A. and Stauffer, D. (2006) On improving 4-km mesoscale model simulations. *Journal of Applied Meteorology and Climatology*, 45, 361–381.

Dipankar, A., Stevens, B., Heinze, R., Moseley, C., Zaengl, G., Giorgetta, M. and Brdar, S. (2015) Large-eddy simulation using the general circulation model ICON. *Journal of Advances in Modeling Earth Systems*, 7, 963–986.

Doms, G. and Baldauf, M. (2015). A description of the non-hydrostatic regional model LM. Part I: Dynamics and Numerics. Consortium for Small-Scale Modelling, Deutscher Wetterdienst, Offenbach, Germany.

Doms, G., Foerstner, J., Heise, E., Herzog, H.-J., Mironov, D., Raschendorfer, M., Reinhardt, T., Ritter, B., Schrodin, R., Schulz, J.-P. and Vogel, G. (2011). A description of the non-hydrostatic COSMO model. Part II: Physical Parameterization. Consortium for Small-Scale Modelling, Deutscher Wetterdienst, Offenbach, Germany.

Errico, R.M. (1985) Spectra computed from a limited-area grid. *Monthly Weather Review*, 113, 1554–1562.

Fritsch, J.M. and Chappell, C.F. (1980) Numerical prediction of convectively driven mesoscale pressure systems. Part I: convective parameterizations. *Journal of Atmospheric Sciences*, 37, 1722–1733.

Gassmann, A. (2011) Inspection of hexagonal and triangular C-grid discretizations of the shallow-water equations. *Journal of Computational Physics*, 230, 2706–2721.

Gassmann, A. (2013) A global hexagonal C-grid non-hydrostatic dynamical core (ICON-IAP) designed for energetic consistency. *Quarterly Journal of the Royal Meteorological Society*, 139, 152–175.

Gassmann, A. and Herzog, H.-J. (2007) A consistent time-split numerical scheme applied to the non-hydrostatic compressible equations. *Monthly Weather Review*, 135, 20–36.

Gassmann, A. and Herzog, H.-J. (2008) Towards a consistent numerical compressible non-hydrostatic model using generalized Hamiltonian tools. *Quarterly Journal of the Royal Meteorological Society*, 134, 1597–1613.

Gerard, L. (2015) Bulk mass-flux perturbation formulation for a unified approach of deep convection at high resolution. *Monthly Weather Review*, 143, 4038–4063.

Gerard, L. and Geleyn, J.-F. (2005) Evolution of a subgrid deep convection parametrization in a limited-area model with increasing resolution. *Quarterly Journal of the Royal Meteorological Society*, 131, 2293–2312.

Giorgetta, M.A., Brokopf, R., Crueger, T., Esch, M., Fiedler, S., Helmert, J., Hohenegger, C., Kornblueh, L., Köhler, M., Manzini, E., Mauritsen, T., Nam, C., Raddatz, T., Rast, S., Reinert, D., Sakradzija, M., Schmidt, H., Schneck, R., Schnur, R., Silvers, L., Wan, H., Zaengl, G. and Stevens, B. (2018) ICON-A, the atmosphere component of the ICON Earth system model. Part I: model description. *Journal of Advances in Modeling Earth Systems*, 10, 1613–1637.

Grabowski, W.W. (2001) Coupling cloud processes with the large-scale dynamics using the cloud-resolving convection parameterization (CRCP). *Journal of the Atmospheric Sciences*, 58, 978–997.

Grabowski, W.W. and Smolarkiewicz, P.K. (1999) CRCP: a cloud-resolving convection parameterization for modeling the tropical convective atmosphere. *Physica D: Nonlinear Phenomena*, 133, 171–178.

Gray, M. (1999) An investigation into convectively generated potential-vorticity anomalies using a mass-forcing model. *Quarterly Journal of the Royal Meteorological Society*, 125, 1589–1605.

Gray, M., Shutts, G.J. and Craig, G. (1998) The role of mass transfer in describing the dynamics of mesoscale convective systems. *Quarterly Journal of the Royal Meteorological Society*, 124, 1183–1207.

Grell, G.A. and Freitas, S.R. (2014) A scale and aerosol aware stochastic convective parameterization for weather and air quality modeling. *Atmospheric Chemistry and Physics*, 14, 5233–5250.

Han, J., Wang, W., Kwon, Y.C., Hong, S.-Y., Tallapragada, V. and Yang, F. (2017) Updates in the NCEP GFS cumulus convection schemes with scale and aerosol awareness. *Weather and Forecasting*, 32, 2005–2017.

Heinze, R., Dipankar, A., Henken, C.C., Moseley, C., Sourdeval, O., Trömel, S., Xie, X., Adamidis, P., Ament, F., Baars, H., Barthlott, C., Behrendt, A., Blahak, U., Bley, S., Brdar, S., Brueck, M., Crewell, S., Deneke, H., Di Girolamo, P., Evaristo, R., Fischer, J., Frank, C., Friederichs, P., Gcke, T., Gorges, K., Hande, L., Hanke, M., Hansen, A., Hege, H.-C., Hoose, C., Jahns, T., Kalthoff, N., Klocke, D., Kneifel, S., Knippertz, P., Kuhn, A., van Laar, T., Macke, A., Maurer, V., Mayer, B., Meyer, C.I., Muppa, S.K., Neggers, R.A.J., Orlandi, E., Pantillon, F., Pospichal, B., Rber, N., Scheck, L., Seifert, A., Seifert, P., Senf, F., Siligam, P., Simmer, C., Steinke, S., Stevens, B., Wapler, K., Weniger, M., Wulfmeyer, V., Zaengl, G., Zhang, D. and Quaas, J. (2017) Large-eddy simulations over Germany using ICON: a comprehensive evaluation. *Quarterly Journal of the Royal Meteorological Society*, 143, 69–100.

Holloway, C., Woolnough, S. and Lister, G. (2012) Precipitation distributions for explicit versus parametrized convection in a large-domain high-resolution tropical case-study. *Quarterly Journal of the Royal Meteorological Society*, 138, 1692–1708.

Holloway, C.E., Woolnough, S.J. and Lister, G.M. (2013) The effects of explicit versus parameterized convection on the MJO in a large-domain high-resolution tropical case study. Part I: characterization of large-scale organization and propagation. *Journal of the Atmospheric Sciences*, 70, 1342–1369.

Holton, J.R. and Hakim, G.J. (2013) *An Introduction to Dynamic Meteorology*. Academic Press, Cambridge, MA.

Jablonowski, C. and Williamson, D.L. (2006) A baroclinic instability test case for atmospheric model dynamical cores. *Quarterly Journal of the Royal Meteorological Society*, 132, 2943–2975.

Kain, J.S. (2004) The Kain–Fritsch convective parameterization: An update. *Journal of Applied Meteorology and Climatology*, 43, 170–181.

Kain, J.S. and Fritsch, J.M. (1990) A one-dimensional entraining/detraining plume model and its application in convective parameterization. *Journal of Atmospheric Sciences*, 47, 2784–2802.

Kain, J.S. and Fritsch, J.M. (1993) Convective parameterization for mesoscale models: the Kain–Fritsch scheme. *Meteorological Monographs*, 24, 165–170.

Kain, J.S., Weiss, S.J., Bright, D.R., Baldwin, M.E., Levit, J.J., Carbin, G.W., Schwartz, C.S., Weisman, M.L., Droegemeier, K.K., Weber, D.B. and Thomas, K.W. (2008) Some practical considerations regarding horizontal resolution in the first generation of operational convection-allowing NWP. *Weather and Forecasting*, 23, 931–952.

Kuell, V. and Bott, A. (2008) A hybrid convection scheme for use in non-hydrostatic numerical weather prediction models. *Meteorologische Zeitschrift*, 17, 775–783.

Kuell, V. and Bott, A. (2009) Application of the hybrid convection parameterization scheme HYMACS to different meteorological situations. *Atmospheric Research*, 94, 743–753. https://doi.org/10.1016/j.atmosres.2009.04.002

Kuell, V. and Bott, A. (2011) Simulation of non-local effects of convection with the hybrid mass flux convection scheme HYMACS. *Meteorologische Zeitschrift*, 20, 227–241.

Kuell, V. and Bott, A. (2019) A physical subgrid-scale information exchange (PSIE) system for parametrization schemes in numerical weather prediction models. *Quarterly Journal of the Royal Meteorological Society*, 145, 767–783.

Kuell, V., Gassmann, A. and Bott, A. (2007) Towards a new hybrid cumulus parametrization scheme for use in non-hydrostatic weather prediction models. *Quarterly Journal of the Royal Meteorological Society*, 133, 479–490.

Kwon, Y.C. and Hong, S.-Y. (2017) A mass-flux cumulus parameterization scheme across gray-zone resolutions. *Monthly Weather Review*, 145, 583–598.

Lane, T.P. and Zhang, F. (2011) Coupling between gravity waves and tropical convection at mesoscales. *Journal of the Atmospheric Sciences*, 68, 2582–2598.

Lauritzen, P.H., Mirin, A.A., Truesdale, J., Raeder, K., Anderson, J.L., Bacmeister, J. and Neale, R.B. (2012) Implementation of new diffusion/filtering operators in the CAM-FV dynamical core. *International Journal of High-Performance Computing Applications*, 26, 63–73.

Lean, H.W., Clark, P.A., Dixon, M., Roberts, N.M., Fitch, A., Forbes, R. and Halliwell, C. (2008) Characteristics of high-resolution versions of the Met Office Unified Model for forecasting convection over the United Kingdom. *Monthly Weather Review*, 136, 3408–3424.

Malardel, S. and Bechtold, P. (2019) The coupling of deep convection with the resolved flow via the divergence of mass flux in the IFS. *Quarterly Journal of the Royal Meteorological Society*, 145, 1832–1845. https://doi.org/10.1002/qj.3528

Malardel, S. and Wedi, N.P. (2016) How does subgrid-scale parametrization influence nonlinear spectral energy fluxes in global NWP models?. *Journal of Geophysical Research: Atmospheres*, 121, 5395–5410.

Mapes, B.E., Warner, T.T. and Xu, M. (2003) Diurnal patterns of rainfall in northwestern South America. Part III: diurnal gravity waves and nocturnal convection offshore. *Monthly weather review*, 131, 830–844.

Marsham, J.H., Dixon, N.S., Garcia-Carreras, L., Lister, G.M., Parker, D.J., Knippertz, P. and Birch, C.E. (2013) The role of moist convection in the West African monsoon system: insights from continental-scale convection-permitting simulations. *Geophysical Research Letters*, 40, 1843–1849.

Miyakawa, T., Satoh, M., Miura, H., Tomita, H., Yashiro, H., Noda, A.T., Yamada, Y., Kodama, C., Kimoto, M. and Yoneyama, K. (2014) Madden–Julian Oscillation prediction skill of a new-generation global model demonstrated using a supercomputer. *Nature Communications*, 5, 3769

Narcowich, F.J. and Ward, J.D. (1994) Generalized Hermite interpolation via matrix-valued conditionally positive definite functions. *Mathematics of Computation*, 63, 661–687.

Ong, H., Wu, C.-M. and Kuo, H.-C. (2017) Effects of artificial local compensation of convective mass flux in the cumulus parameterization. *Journal of Advances in Modeling Earth Systems*, 9, 1811–1827.

Park, S. (2014) A unified convection scheme (UNICON). Part I: formulation. *Journal of the Atmospheric Sciences*, 71, 3902–3930.

Pearson, K., Lister, G., Birch, C., Allan, R., Hogan, R. and Woolnough, S. (2014) Modelling the diurnal cycle of tropical convection across the 'grey zone'. *Quarterly Journal of the Royal Meteorological Society*, 140, 491–499.

Plant, R.S. and Craig, G.C. (2008) A stochastic parameterization for deep convection based on equilibrium statistics. *Journal of Atmospheric Sciences*, 65, 87–105.

Prill, F., Reinert, D., Rieger, D., Zaengl, G., Schroeter, J., Foerstner, J., Werchner, S., Weimer, M., Ruhnke, R. and Vogel, B. (2019) *Working with the ICON Model – Practical exercises for NWP mode and ICON-ART*. ICON Model Tutorial, Deutscher Wetterdienst, Offenbach, Germany.

Rieger, D. (2018). http://www.cosmo-model.org/content/tasks/priorityProjects/c2i/default.htm; accessed 5 April 2020.

Rípodas, P., Gassmann, A., Forstner, J., Majewski, D., Giorgetta, M., Korn, P., Kornblueh, L., Wan, H., Zaengl, G., Bonaventura, L. and Heinze, T. (2009) Icosahedral shallow-water model (ICOSWM): results of shallow-water test cases and sensitivity to model parameters. *Geoscientific Model Development*, 2, 231–251.

Skamarock, W.C. (2011). Kinetic energy spectra and model filters, pp. 495–512 in Numerical Techniques for Global Atmospheric Models. Lauritzen, P.H., Jablonowski, C., Taylor, M.A., Nair, R.D. (eds), Springer, Berlin.

Skamarock, W.C. and Klemp, J.B. (1992) The stability of time-split numerical methods for the hydrostatic and the nonhydrostatic elastic equations. *Monthly Weather Review*, 120, 2109–2127.

Staniforth, A. and Thuburn, J. (2012) Horizontal grids for global weather and climate prediction models: a review. *Quarterly Journal of the Royal Meteorological Society*, 138, 1–26.

Stein, T.H.M., Parker, D.J., Hogan, R.J., Birch, C.E., Holloway, C.E., Lister, G.M., Marsham, J.H. and Woolnough, S.J. (2015) The representation of the West African monsoon vertical cloud structure in the Met Office Unified Model: an evaluation with CloudSat. *Quarterly Journal of the Royal Meteorological Society*, 141, 3312–3324. https://doi.org/10.1002/qj.2614

Thuburn, J., Weller, H., Vallis, G.K., Beare, R.J. and Whitall, M. (2018) A framework for convection and boundary-layer parameterization derived from conditional filtering. *Journal of the Atmospheric Sciences*, 75, 965–981.

Tiedtke, M. (1989) A comprehensive mass flux scheme for cumulus parameterization in large-scale models. *Monthly Weather Review*, 117, 1779–1800.

Tiedtke, M. (1993) Representation of clouds in large-scale models. *Monthly Weather Review*, 121, 3040–3061.

Tomita, H. and Satoh, M. (2004) A new dynamical framework of non-hydrostatic global model using the icosahedral grid. *Fluid Dynamics Research*, 34, 357

Tomita, H., Tsugawa, M., Satoh, M. and Goto, K. (2001) Shallow-water model on a modified icosahedral geodesic grid by using spring dynamics. *Journal of Computational Physics*, 174, 579–613.

Ullrich, P.A., Jablonowski, C., Kent, J., Lauritzen, P.H., Nair, R., Reed, K.A., Zarzycki, C.M., Hall, D.M., Dazlich, D., Heikes, R., Konor, C., Randall, D., Dubos, T., Meurdesoif, Y., Chen, X., Harris, L., Kühnlein, C., Lee, V., Qaddouri, A., Girard, C., Giorgetta, M., Reinert, D., Klemp, J., Park, S.-H., Skamarock, W., Miura, H., Ohno, T., Yoshida, R., Walko, R., Reinecke, A. and Viner, K. (2017) DCMIP2016: a review of non-hydrostatic dynamical core design and intercomparison of participating models. *Geoscientific Model Development*, 10, 4477–4509. https://doi.org/10.5194/gmd-10-4477-2017

Wan, H. (2009). Developing and testing a hydrostatic atmospheric dynamical core on triangular grids. PhD thesis, Max Planck Institute for Meteorology, Hamburg, Germany.

Wan, H., Giorgetta, M.A., Zaengl, G., Restelli, M., Majewski, D., Bonaventura, L., Froehlich, K., Reinert, D., Ripodas, P., Kornblueh, L. and Foerstner, J. (2013) The ICON-1.2 hydrostatic atmospheric dynamical core on triangular grids, Part I: formulation and performance of the baseline version. *Geoscientific Model Development*, 6, 735–763.

Weisman, M.L., Davis, C., Wang, W., Manning, K.W. and Klemp, J.B. (2008) Experiences with 0–36 h explicit convective forecasts with the WRF-ARW model. *Weather and Forecasting*, 23, 407–437.

Wolfram, P.J. and Fringer, O.B. (2013) Mitigating horizontal divergence "checkerboard" oscillations on unstructured triangular C-grids for nonlinear hydrostatic and non-hydrostatic flows. *Ocean Modelling*, 69, 64–78.

Wu, C.-M. and Arakawa, A. (2014) A unified representation of deep moist convection in numerical modeling of the atmosphere. Part II. *Journal of the Atmospheric Sciences*, 71, 2089–2103.

Yano, J.-I., Bister, M., Fuchs, Ž., Gerard, L., Phillips, V., Barkidija, S. and Piriou, J.-M. (2013) Phenomenology of convection–parameterization closure. *Atmospheric Chemistry and Physics*, 13, 4111–4131.

Zaengl, G., Reinert, D., Rípodas, P. and Baldauf, M. (2015) The ICON (ICOsahedral Non-hydrostatic) modelling framework of DWD and MPI-M: description of the non-hydrostatic dynamical core. *Quarterly Journal of the Royal Meteorological Society*, 141, 563–579.

Zdunkowski, W. and Bott, A. (2003) *Dynamics of the Atmosphere: A Course in Theoretical Meteorology*. Cambridge University Press, Cambridge, UK.

APPENDIX A: CONSERVATIVE DISCRETIZATION OF CONVECTIVE ψ-TENDENCIES

In the following section, we will briefly demonstrate that the discretized form of the convective ψ-tendency given by Equation (7) is conservative.

Assuming a simple experimental set-up where a passive tracer is initially only present in a source layer of depth $\Delta z(k_{src}) = \Delta z_1$ with a specific content $q_{tr}(k_{src}, t_0)$, the total amount of the passive tracer $m_{tr}(t_0)$ can be calculated by

$$m_{tr}(t_0) = \rho(k_{src}, t_0)\, q_{tr}(k_{src}, t_0)\, A\, \Delta z_1, \qquad (A1)$$

where $\rho(k_{src}, t_0)$ denotes the initial density of the source layer and A is the horizontal area of a particular grid box. Let M_{conv} be the convective flux (in $\mathrm{kg\,s^{-1}}$) which

transports air from the source layer k_{src} to an arbitrary detrainment layer k_{end} with a layer depth $\Delta z(k_{end}) = \Delta z_2$. Then, according to Equation (2), the convective density tendencies in the two layers are given by

$$\left.\frac{\partial \rho}{\partial t}\right|_{conv}(k_{src}) = -\frac{M_{conv}}{A\Delta z_1},$$

$$\left.\frac{\partial \rho}{\partial t}\right|_{conv}(k_{end}) = \frac{M_{conv}}{A\Delta z_2} = -\left.\frac{\partial \rho}{\partial t}\right|_{conv}(k_{src})\frac{\Delta z_1}{\Delta z_2}. \quad \text{(A2)}$$

Using Equation (7) with $\epsilon_u = 0$, the tendency of the specific tracer content q_{tr} in the detrainment layer k_{end} can be written compactly as

$$\left.\frac{\partial q_{tr}}{\partial t}\right|_{conv}(k_{end}) = \frac{1}{A\Delta z_2}\frac{M_{conv}q_{tr}(k_{src},t_0)}{\rho^\star(k_{end})}, \quad \text{(A3)}$$

where $\rho^\star(k_{end})$ is the updated density due to the parametrized net mass transfer (Equation (A4)). Note that the draught transports air with the specific tracer content of the source layer whose tracer concentration remains constant due to homogeneous mixing, i.e., $q_{tr}(k_{src}) = \text{const}$.

Thus, the total tracer amount after a convective transport over a time period Δt is given by

$$m_{tr}(t_0+\Delta t) = \rho^\star(k_{src}) \, q_{tr}(k_{src},t_0) \, A\Delta z_1$$
$$+ \rho^\star(k_{end}) \, q_{tr}^\star(k_{end}) \, A\Delta z_2$$
$$= \rho(k_{src},t_0) \, q_{tr}(k_{src},t_0) \, A\Delta z_1 - M_{conv} \, q_{tr}(k_{src},t_0)\Delta t$$
$$+ \rho^\star(k_{end})\frac{M_{conv}q_{tr}(k_{src},t_0)}{\rho^\star(k_{end})}\Delta t,$$

$$\text{with } \psi^\star(k) = \psi(t_0)(k) + \left.\frac{\partial \psi}{\partial t}\right|_{conv}(k)\Delta t; \quad \psi \in \{\rho, q_{tr}\}.$$
$$\text{(A4)}$$

Since the last two terms cancel each other, the total tracer amount remains constant in the presense of convective transports, i.e., $m_{tr}(t_0) = m_{tr}(t_0+\Delta t)$.

This simplified transport experiment can easily be extended to more complex situations with variable entrainment/detrainment profiles and variable tracer concentrations. Thus, it is confirmed that Equation (7) obeys the conservation law of a balance equation.

APPENDIX B: CONVECTIVE EXNER TENDENCY

Internally, HYMACS operates on density, enthalpy and the specific moisture content as prognostic variables. The corresponding convective tendencies are passed to the hosting model. Since the first law of thermodynamics in ICON is given in terms of the Exner pressure (rather than enthalpy), a corresponding convective π-tendency in Equation (13) has to be calculated.

We start by reformulating the Exner pressure beforehand with the help of the equation of state and the definition equation for the virtual potential temperature. By subsequent logarithmic differentation of π using the general differential operator δ, we get

$$\pi = \left(\frac{p}{p_{00}}\right)^\gamma = \left(\frac{R_d\rho T_v}{p_{00}}\right)^\gamma,$$

$$\Rightarrow \frac{1}{\pi}\delta\pi = \frac{\gamma}{p}\delta p = \frac{\gamma}{\rho T}\delta(\rho T) + \frac{\gamma}{1+\alpha}\delta\alpha, \quad \text{(B1)}$$

where $\gamma = R_d/c_{pd}$ was introduced for convenience.

Setting $\delta = d/dt$, the two expressions in the second row can be used to rewrite the first law of thermodynamics in terms of the Exner pressure given by

$$c_p\frac{d}{dt}(\rho T) - c_p T\frac{d\rho}{dt} - \frac{dp}{dt} = Q_{h,dia}$$
$$= Q_{h,noconv} + \left.\rho\frac{\partial h}{\partial t}\right|_{conv}. \quad \text{(B2)}$$

Note that the diabatic enthalpy term $Q_{h,dia}$ on the right-hand side was split in order to introduce the convective enthalpy tendency provided by HYMACS. Then, additional application of the equation of state and $R_d(1+\alpha) = c_p - c_v$ yields

$$\frac{1}{\gamma\pi}\frac{d\pi}{dt} = \frac{c_p}{c_v}\left(\frac{1}{1+\alpha}\frac{d\alpha}{dt} + \frac{1}{\rho}\frac{d\rho}{dt} + \frac{Q_{h,noconv}}{\rho c_p T} + \left.\frac{1}{c_p T}\frac{\partial h}{\partial t}\right|_{conv}\right). \quad \text{(B3)}$$

After some further algebraic steps, we proceed by replacing the individual derivative terms according to the prognostic equations used with HYMACS in ICON.

In the model, the individual change in π comprises the local Exner pressure tendency and a grid-scale advection term. For $d\rho/dt$, we use the continuity equation and rewrite Equation (22) by

$$\frac{d\rho}{dt} = -\rho\nabla\cdot\mathbf{v} + \left.\frac{\partial\rho}{\partial t}\right|_{conv}. \quad \text{(B4)}$$

Finally, using the budget equation for the moisture species (Equation (14) with the convective sources added on the right-hand side) for $\rho(d\alpha/dt)$ with

$$\left.\rho\frac{\partial\alpha}{\partial t}\right|_{conv} = \rho\left\{\left(\frac{R_v}{R_d}-1\right)\left.\frac{\partial q_v}{\partial t}\right|_{conv} - \left.\frac{\partial q_{cond}}{\partial t}\right|_{conv}\right\}, \quad \text{(B5)}$$

we end up with

$$\frac{c_{vd}}{c_{pd}}\rho\,\theta_v\frac{\partial\pi}{\partial t} + c_{pd}\pi\nabla\cdot(\rho\,\theta_v\mathbf{v}) - c_{pd}\pi\rho\,\theta_v(\nabla\cdot\mathbf{v})$$

$$
= \frac{c_p c_{vd}}{c_v} \left\{ \frac{T_v}{(1+\alpha)} \left(S_{\alpha,\text{noconv}} + \rho \frac{\partial \alpha}{\partial t} \bigg|_{\text{conv}} \right) \right.
$$

$$
\left. + T_v \frac{\partial \rho}{\partial t} \bigg|_{\text{conv}} - \rho T_v (\nabla \cdot \mathbf{v}) \right\}
$$

$$
+ \frac{c_{vd}}{c_v} (1+\alpha) \left(Q_{h,\text{noconv}} + \rho \frac{\partial h}{\partial t} \bigg|_{\text{conv}} \right). \tag{B6}
$$

Note that the advection term of π was reformulated with the help of another identity for the Exner pressure

$$
\pi = \left(\frac{R_d}{p_{00}} \rho \theta_v \right)^{\frac{R_d}{c_{vd}}},
$$

$$
\Rightarrow \delta \pi = \frac{R_d}{c_{vd}} \frac{\pi}{\rho \theta_v} \delta(\rho \theta_v). \tag{B7}
$$

After rearranging Equation (B6) in order to isolate the local Exner pressure tendency on the left-hand side and after approximating the specific heat capacities for moist air by c_{pd} and c_{vd}, we are ready to collect the convective π-tendencies:

$$
\frac{\partial \pi}{\partial t} = -c_{pd} \pi \nabla \cdot (\rho \, \theta_v \mathbf{v}) + Q_{\pi,\text{noconv}} + \frac{R_d}{c_{vd}}
$$

$$
\times \left(\frac{(1+\alpha)}{c_{pd} \theta_v} \frac{\partial h}{\partial t} \bigg|_{\text{conv}} + \frac{\pi}{(1+\alpha)} \frac{\partial \alpha}{\partial t} \bigg|_{\text{conv}} + \frac{\pi}{\rho} \frac{\partial \rho}{\partial t} \bigg|_{\text{conv}} \right). \tag{B8}
$$

The first two terms provide local π-tendencies due to divergence of the grid-scale θ_v-fluxes and due to non-convective diabatic processes whose effect is cast in $Q_{\pi,\text{noconv}}$. As desired, the terms in the second row allow a computation of the convective π-tendencies in terms of the tendencies provided by HYMACS.